



## Engineered a dual-targeting HA-TPP/A nanoparticle for combination therapy against *KRAS-TP53* co-mutation in gastrointestinal cancers

Yong Mei<sup>a,1</sup>, Xiaohua Qin<sup>b,1</sup>, Zhenyu Yang<sup>b</sup>, Shiyao Song<sup>a</sup>, Xiaoting Liu<sup>a</sup>, Chong Wu<sup>a</sup>, Jieying Qian<sup>b</sup>, Xiaowan Huang<sup>b</sup>, Yunjiao Zhang<sup>b,d,\*\*</sup>, Weiling He<sup>a,c,\*</sup>

<sup>a</sup> Department of Gastrointestinal Surgery, The First Affiliated Hospital, Sun Yat-Sen University, Guangzhou, Guangdong, 510080, China

<sup>b</sup> School of Biomedical Science and Engineering, School of Medicine, South China University of Technology, Guangzhou, Guangdong, 510006, China

<sup>c</sup> Department of Gastrointestinal Surgery, Xiang'an Hospital of Xiamen University, School of Medicine, Xiamen University, Xiamen, Fujian, 361000, China

<sup>d</sup> National Engineering Research Centre for Tissue Restoration and Reconstruction and Key Laboratory of Biomedical Engineering of Guangdong Province, South China University of Technology, Guangzhou, Guangdong, 510006, China

### ARTICLE INFO

#### Keywords:

Dual-targeting  
KRAS  
TP53  
Co-mutation  
HA-TPP/A nanoparticle  
Mitochondrial targeting  
Gastrointestinal cancer

### ABSTRACT

*KRAS-TP53* co-mutation is strongly associated with poor prognosis and high malignancy in gastrointestinal cancers. Therefore, a novel approach to oncotherapy may lie in combination therapy targeting both *KRAS* and *TP53*. Herein, we present a novel self-assembled nanoparticle (HA-TPP/A) that are functionalized nano-carrier hyaluronic acid (HA)-TPP conjugate (HA-TPP) to degrade mutant p53 proteins (mutp53) and co-deliver AMG510 for treating *KRAS-TP53* co-alteration of gastrointestinal cancers by inhibiting the mutant *KRAS* and mutp53 signaling pathways. The HA-TPP/A nanoparticles led to ubiquitination-dependent proteasomal degradation of mutp53 by targeting damage to mitochondria. Furthermore, these nanoparticles abrogated the gain-of-function (GOF) phenotypes of mutp53 and increased sensitivity to AMG510-induced cell killing, thereby reducing cell proliferation and migration in gastrointestinal cancer with *KRAS-TP53* co-mutation. The co-loaded HA-TPP/A nanoparticles demonstrated remarkable therapeutic efficacy in a tumor-bearing mouse model, particularly in *KRAS-TP53* double mutant expressing cancer cells, compared with single drug and combined free drug groups. Notably, HA-TPP/A is the first reported nanoparticle with an ability to co-target *KRAS-TP53*, providing a promising approach for therapy in highly malignant gastrointestinal tumors and potentially expanding clinical indications for AMG510 targeted therapies in gastrointestinal tumors.

### 1. Introduction

Gastrointestinal cancers are the leading cause of cancer death around the world and represent more than one-fourth of all cancer incidence and one-third of cancer-related mortality [1]. Among them, colorectal cancer (CRC) is the third most common cause of cancer mortality worldwide with a 5-year survival rate of roughly 14 % in an advanced/metastatic stage of the disease [2], while pancreatic ductal adenocarcinoma (PDAC) is a highly aggressive lethal malignancy which has the lowest 5-year relative survival rate of all human cancers [3,4]. The development and progression of these cancers are driven by the

accumulation of “driver” mutations, such as *KRAS*, *PIK3CA*, *SMAD4*, and *TP53* [5], which promote tumorigenesis and lead to tumor drug resistance, recurrence, and metastasis.

Of these mutations, *KRAS* is one of the most commonly mutated oncogenes in gastrointestinal cancers [6,7], with downstream signaling pathways promoting cancer progression [8,9], and has long been considered “undruggable” [10,11] due to its nearly spherical structure, lack of a deep hydrophobic pocket, and absence of an obvious binding site [12]. Patients with *KRAS*<sup>G12C</sup>-mutated CRC have worse outcomes than patients with other *KRAS* mutations [7,13–15], and *KRAS*<sup>G12C</sup> tumors are associated with tumor mutational burden-high status [16].

Peer review under responsibility of KeAi Communications Co., Ltd.

\* Corresponding author. Department of Gastrointestinal Surgery, The First Affiliated Hospital, Sun Yat-sen University, Guangzhou, Guangdong, 510080, China.

\*\* Corresponding author. School of Biomedical Science and Engineering, School of Medicine, South China University of Technology, Guangzhou, Guangdong, 510006, China.

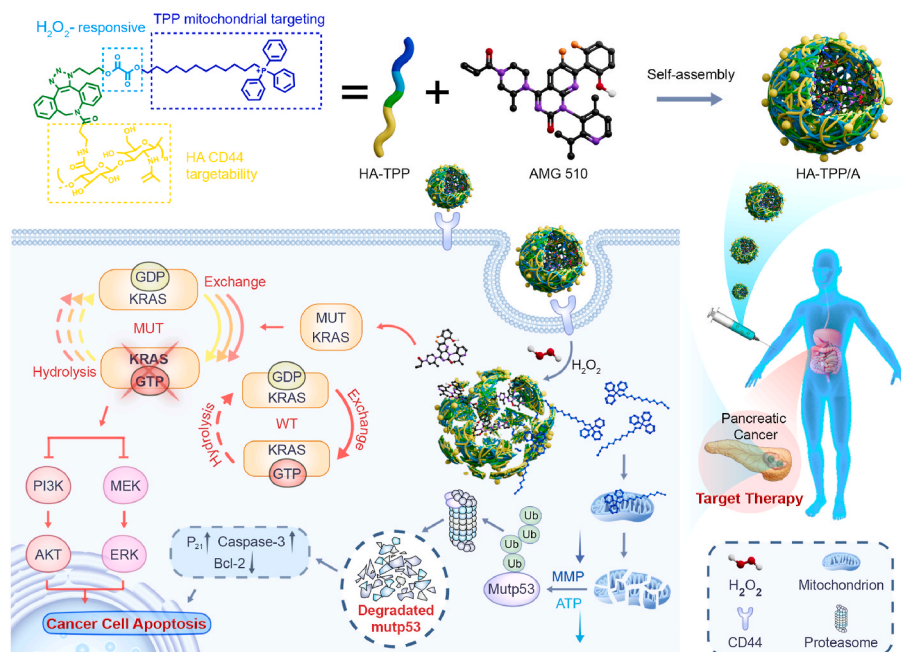
E-mail addresses: [zhangyunjiao@scut.edu.cn](mailto:zhangyunjiao@scut.edu.cn) (Y. Zhang), [hewling@mail.sysu.edu.cn](mailto:hewling@mail.sysu.edu.cn) (W. He).

<sup>1</sup> These authors contributed equally to this work.

<https://doi.org/10.1016/j.bioactmat.2023.10.003>

Received 6 July 2023; Received in revised form 19 September 2023; Accepted 3 October 2023

2452-199X/© 2023 The Authors. Publishing services by Elsevier B.V. on behalf of KeAi Communications Co. Ltd. This is an open access article under the CC BY-NC-ND license (<http://creativecommons.org/licenses/by-nc-nd/4.0/>).



**Scheme 1.** The schematic illustration of HA-TPP/A nanoheterojunctions with well-controlled morphology as novel dual-targeting nanoparticle and its great synergistic effects for treating *KRAS-TP53* co-alteration of gastrointestinal cancers by inhibiting the mutant *KRAS* and *mutp53* signaling pathways.

Recent clinical trials have shown promise for *KRAS*<sup>G12C</sup> inhibitors, such as AMG510, in treating multiple tumors harboring this genetic mutation [17,18] and was first approved by the U.S. FDA for the treatment of adult patients with non-small cell lung cancer (NSCLC), although drug resistance and limited activity in gastrointestinal cancers remain a challenge [19,20]. Furthermore, the high resistance of AMG510 to monotherapy in the short term is a cause for concern [21–23]. The possible reason is that the clinical relevance of cancer is not only reflected in the frequent mutations of *KRAS* but also the frequent alterations in other genes. In particular, *KRAS-TP53* co-alteration is associated with cancer metastasis, worse survival and immune exclusion in human CRC and PDAC [24,25]. Therefore, combined treatment of multiple key targets may be a vital measure to overcome drug resistance.

Mutations in *TP53* are also prevalent in gastrointestinal cancers and can confer oncogenic gain-of-function (GOF) activities that contribute to poor prognosis and drug resistance [26,27]. Therefore, multiple treatments for mutant p53 proteins (*mutp53*) targeted tumors have been proposed, including the transformation of *mutp53* to wild-type p53 proteins (*wtp53*), restoration of *wtp53* expression, and elimination of *mutp53*. Of these strategies, the elimination of *mutp53* is probably the most straightforward strategy [28–30], and various agents being reported gradually in recent years, including small molecules and nanomaterials [31–34]. Unfortunately, these latest studies eliminated mutant p53, were unable to regulate oncogenic *KRAS* simultaneously, limiting the extensive applications in treating p53-*KRAS*-double-mutated PDAC. A large amount of evidence points out that GOF of *mutp53* is closely related to oxidative stress [35–37], and a high level of GSH is indispensable to scavenge excessive ROS and detoxify xenobiotics in cancer cells [38]. In our previous reports, we found that targeting mitochondria to regulate cell redox state and tune the ratio between intracellular reduced glutathione (GSH) and oxidized glutathione (GSSG) was essential for *mutp53* glutathionylation and degradation [33,39].

Mitochondria is recognized as one of the most important targets for new drug design in cancer [40,41], and the most effective way to deliver drugs specifically to mitochondria is by covalent linking a lipophilic cation such as an alkyltriphenylphosphonium (TPP) moiety to a pharmacophore of interest [42,43]. In recent years, nanomaterial-based carriers have been enormously studied for gene therapy [44]. Based

on these considerations, we conducted innovatively a treatment strategy abrogated the GOF effects exerted by *mutp53* and inhibited downstream signaling pathways regulated mutant *KRAS*. In this study, we investigated the potential of a mitochondria-targeted functionalized nano-carrier hyaluronic acid (HA)-TPP conjugate (HA-TPP) to degrade *mutp53* protein and co-deliver AMG510, and developed a novel self-assembled nanoparticles (HA-TPP/A) for co-targeting treatment of gastrointestinal cancer. By incorporating HA in HA-TPP/A improved the delivery of TPP and AMG510 to tumor cells with rich CD44 receptors [45–47]. Our findings provide a novel solution to the co-mutation of *KRAS* and *TP53* and offer new insights into the development of dual-targeting combination therapy for gastrointestinal cancers (Scheme 1).

## 2. Methods

### 2.1. Materials

TPP were provided by Aladdin Bio-Chem Technology Co., Ltd. Dibenzocyclooctyne-amine-TFA (DBCO-amine-TFA) was purchased from Biomatrik Inc. HA sodium salt (90 kDa) was provided by Dongyuan Biology Technology Co., Ltd. AMG510, Cycloheximide, CQ, MG132, PYR41 and 3MA were purchased from Selleck Chemicals. The sources of antibodies used in this experiment were as follows: Anti-p53 (Abcam, sc-126), anti-GAPDH (Chemicon, AB9132), K48-linkage specific polyubiquitin antibody (Cell Signaling Technology, 1280S), anti-p44/42 MAPK (ERK1/2) (Cell Signaling Technology, 4695S), anti-phospho-p44/42 MAPK (p-ERK1/2) (Cell Signaling Technology, 4370S), anti-AKT (Cell Signaling Technology, 4691S), anti-phospho-AKT S473 (Cell Signaling Technology, 4060S), anti-p21 (Abcam, ab227443), anti-Bcl-2 (Cell Signaling Technology, 15071), anti-Cleaved Caspase-3 (Cell Signaling Technology, 9661S), HRP conjugated anti-rabbit IgG (Promega, W4011), HRP-conjugated anti-mouse IgG (Promega, W4021).

### 2.2. Synthesis of 3-azidopropan-1-ol

3-bromopropan-1-ol (1.39 g, 10 mmol) was dissolved in 25 mL deionized water, followed by addition of sodium azide (1.95 g, 30

mmol). The mixture was stirred at 60 °C for 48 h. After cooling to room temperature, the reaction mixture was extracted with dichloromethane (50 mL × 3). The combined organic phase was dried over anhydrous magnesium sulfate and concentrated under reduced pressure to yield 3-bromopropan-1-ol as light yellow oil (0.91 g, yield 90 %). <sup>1</sup>H NMR (400 MHz, Chloroform-*d*) δ (ppm) = 3.76 (t, *J* = 6.0 Hz, 2H), 3.45 (t, *J* = 6.6 Hz, 2H), 1.83 (p, *J* = 6.3 Hz, 2H). <sup>13</sup>C NMR (400 MHz, Chloroform-*d*) δ (ppm) = 31.45, 49.03, 58.25.

### 2.3. Synthesis of 12-hydroxydodecyl triphenylphosphonium (2a)

12-Bromododecanol (2.65 g, 10 mmol) and triphenylphosphine (5.25 g, 20 mmol) were dissolved in 50 mL acetonitrile. The mixture was stirred at 80 °C for 48 h. After cooling to room temperature, the reaction mixture was concentrated under reduced pressure. The residue was recrystallized with dichloromethane and ethyl acetate to yield 2a as light brown viscous solid (4.53 g, yield 86 %). <sup>1</sup>H NMR (400 MHz, Chloroform-*d*) δ (ppm) = 7.91–7.65 (m, 15H), 3.84–3.72 (m, 2H), 3.62 (t, *J* = 6.6 Hz, 2H), 1.56 (dq, *J* = 27.9, 7.2, 6.7 Hz, 6H), 1.21 (d, *J* = 20.9 Hz, 14H). <sup>13</sup>C NMR (400 MHz, Chloroform-*d*) δ (ppm) = 135.09, 135.07, 135.04, 134.99, 134.97, 133.76, 133.76, 133.72, 133.69, 133.67, 133.66, 130.60, 130.57, 130.53, 130.51, 130.48, 130.45, 118.76, 118.65, 118.19, 118.08, 62.92, 32.75, 30.44, 30.34, 30.23, 29.73, 29.40, 29.33, 29.27, 29.17, 29.10, 28.94, 28.90, 28.81, 26.17, 25.67, 22.96, 22.70, 22.64. HRMS (ESI): *m/z* (M – Br)<sup>+</sup> calcd for C<sub>30</sub>H<sub>40</sub>OP<sup>+</sup>: 447.2811; found: 447.2827.

### 2.4. Synthesis of HA-DBCO

Hyaluronic acid (300 mg) was dissolved in 25 mL deionized water, followed by addition of 1-ethyl-3-(3-dimethylaminopropyl) carbodiimide hydrochloride (671 mg, 3.50 mmol) and N-hydroxysuccinimide (403 mg, 3.50 mmol). After stirred at room temperature for 0.5 h, DBCO-NH<sub>2</sub> (85 mg, 0.39 mmol) in 5 mL DMSO was added to the solution, and the stirred at room temperature for 24 h. The solution was then dialyzed against deionized water/methanol mixture (1:1, v: v) for 24 h and deionized water for additional 48 h, followed by freeze-dried to yield HA-DBCO as light yellow solid.

### 2.5. Synthesis of HA-TPP

Oxalyl chloride (1.27 g, 10.00 mmol) was dissolved in 10 mL anhydrous dichloromethane in the ice water bath, followed by addition of 3-azidopropan-1-ol (202 mg, 2 mmol). The mixture was stirred at 0 °C for 4 h. Then the mixture was evaporated to remove excess oxalic dichloride to obtain an intermediate. The residue was redissolved by 10 mL anhydrous dichloromethane, followed by addition of 2a (527 mg, 1 mmol) and triethylamine (110 mg, 1.1 mmol). After stirred at 0 °C overnight, the reaction mixture was extracted with 1 % HCl. The organic phase was concentrated under reduced pressure. The residue was recrystallized with dichloromethane and ethyl acetate to remove excess 3-azidopropan-1-ol to yield the crude product (12-(2-(3-azidopropoxy)-2-oxoacetoxy)dodecyl) triphenylphosphonium (2b) as brownish-yellow viscous solid.

HA-DBCO (300 mg) was dissolved in 40 mL water/dimethyl sulfoxide mixture (1:4, v:v), then all previously synthesized crude product 2b in 10 mL water/dimethyl sulfoxide mixture (1:4, v:v) was dropped into the solution. After stirred for 48 h, the solution was dialyzed against deionized water/methanol mixture (1:1, v:v) for 24 h and deionized water for additional 48 h, followed by freeze-dried to yield HA-TPP as light yellow solid. <sup>1</sup>H NMR (400 MHz, Chloroform-*d*) δ (ppm) = 7.67 (m, 15H), 7.29 (m, 8H).

### 2.6. Preparation and characterization of HA-TPP/A

HA-TPP/A were prepared by single step emulsion methods [48]. In

brief, AMG510 (1 mg) was dissolved in chloroform (2 mL), while n-HA-oxa-TPP (100 mg) was dissolved in saline (10 mL). The organic phase was dropped into the aqueous phase under sonication using a probe-type ultrasonicator (JY92-IIN, Scientz) for 20 min. The organic solvent in the emulsion was removed under a vacuum using a rotary evaporator (HB-10, IKA). Finally, HA-TPP/A were obtained after filtration through a porous membrane filter (pore size, 220 nm) to remove the non-encapsulated drugs. The encapsulation efficiency (EE%) was calculated based on the below equations: EE (%) = (W<sub>loaded drug</sub>)/(W<sub>total drug</sub>) × 100%. The entrapment efficiency for AMG510 was analyzed via Ultraviolet (UV). Drug quantification of TPP was detected by ICP and UV. The particle size and zeta potential of the nanoparticles were measured using a particle size and zeta potential analyser (Litesizer 500, Anton paar). The morphology of the nanoparticles was characterized using a transmission electron microscope (TEM) conducted on JEM-2100F (JEOL, Japan) and scanning electron microscope (SEM). The stability of HA-TPP/A against serum protein was evaluated by monitoring the size change after incubation with bovine serum albumin (10 mg/mL). In vitro drug release, HA-TPP/A (2 mL) were placed into a dialysis bag (molecular weight cut-off, 3500), which was immersed in the release medium (20 mL) of phosphate-buffered saline (PBS) (pH 6.5) under stirring at 100 rpm under 37 °C. To assess the ROS responsiveness of HA-TPP/A, different concentrations of H<sub>2</sub>O<sub>2</sub> were added into the release medium. The release medium (5 mL) was sampled at pre-determined time points, and the same volume of fresh medium was supplemented. The quantities of AMG510 in the release medium were determined using UV.

### 2.7. Cell culture

Four human CRC cell lines (SW837, HCT8, T84, DLD-1), two human PDAC cell lines (MIA PaCa-2, PATU-8988S), human normal liver cell line (LO2) and human normal colon cell line (HCoEpic) used in this study were purchased from ATCC. SW837, HCT8, T84, MIA PaCa-2, PATU-8988S, LO2 and HCoEpic were cultured in DMEM medium (Gibco, USA). DLD-1 was cultured in RPMI-1640 medium (Gibco, USA). The DMEM medium and RPMI-1640 medium both contain 10 % FBS (Gibco, USA) and 1 % penicillin/streptomycin (Gibco, USA). All cells were incubated in a cell incubator at 37 °C and 5 % CO<sub>2</sub>.

### 2.8. Cellular uptake

MIA PaCa-2 cells were cultured in a 6-well plate at a density of 1 × 10<sup>6</sup> cells per well, followed by treatment with AMG510 or HA-TPP/A for different incubation times (2, 6, and 12 h). After treatments, the cells were washed three times with sterile PBS and then the cells were harvested and digested with chloroform. Finally the amount of AMG510 were measured by UV-vis spectroscopy.

### 2.9. Intracellular mitochondrial membrane potential detection

JC-1 assay kit (Beyotime, China) was used to detect intracellular mitochondrial membrane potential. Cells were seeded in glass-bottom cell culture dishes (1 × 10<sup>5</sup> cells/dish) and then treated with or without HA-TPP/A. After 24 h of incubation, cells were treated with 10 μM JC-1 in the dark at 37 °C under 5 % CO<sub>2</sub> for 30 min. Then fluorescence images were obtained by fluorescence microscopy.

### 2.10. Measurement of ATP activity

An ATP Assay Kit (Beyotime, China) was used to measure the level of ATP in the cell. Cells were seeded in a 6-well plate, after 24 h of dosing, the culture medium was removed and washed gently with PBS. Then 200 μL lysis buffer was added to each well, and the culture plate was repeatedly blown with a pipette or shaken to make the lysis buffer fully contact and lysate the cells. After lysing, centrifuged 12000g at 4 °C for

5 min, supernatant was taken for subsequent determination. Added 20  $\mu\text{L}$  supernatant to 100  $\mu\text{L}$  ATP detection solution and mixed well, then detected by a spectrophotometer (Elx800, Biotek, Winooski, VT, USA). The measured value was relative luminescence unit (RLU).

### 2.11. Cellular ROS detection

The DCFH-DA Assay Kit was used for ROS detection. MIA PaCa-2 cells were cultured at a concentration of  $2 \times 10^5$  cells per well (12-well plates), and were incubated for 24 h. Cells were treated with HA-TPP/A or ROS inhibitors for 12h. The cells were then incubated at 37 °C for 30 min with the DCFH-DA probe (Beyotime, China) in reduced serum media (Opti-MEM TM). After triple washing with PBS, results were detected by flow cytometry (BD, Bioscience).

### 2.12. Cell proliferation assay

Cells were seeded in the 96-well plate and cell proliferation was assessed by MTT (BioFroxx, Germany). After treatments, MTT was added to the growth medium at a ratio of 1:9 and incubated for 4 h at 37 °C under 5 %  $\text{CO}_2$ . Then removed the supernatant, added 150  $\mu\text{L}$  DMSO to each well and shaken for 15 min to fully dissolve the crystals. The absorbance value of each well was measured at the wavelength of 490/570 nm by a spectrophotometer (Elx800, Biotek, Winooski, VT, USA).

### 2.13. Colony formation assay

Cells were seeded on 6-well plates and then treated as following: (1) growth medium (no treatments, as control), (2) AMG510, (3) HA-TPP, (4) AMG510+HA-TPP, (5) HA-TPP/A. After 12 h incubation, then changed to new medium. After culture for another 12 days, colonies were fixed with methanol, stained with 0.1 % of crystal violet for 15 min at room temperature. The colonies were then washed with ddH<sub>2</sub>O and imaged.

### 2.14. Wound-healing assay

Cells were cultured in 6-well plates. When the cells grow to a state of fusion into a monolayer, cells were scratched gently with a p100 pipette tip perpendicular to the cell plane, and then cells were washed three times with sterile PBS to remove scattered cells and made the gaps left by streaking clearly visible, then replaced with fresh medium. Subsequently, the cells were treated as follows: (1) growth medium (no treatments, as control), (2) AMG510, (3) HA-TPP, (4) AMG510+HA-TPP, (5) HA-TPP/A for 24 h. The images of wound healing were taken by the confocal microscope.

### 2.15. Detection of cell apoptosis

Discrimination between apoptosis and necrosis was done by treatment of cells with Annexin V-FITC and PI Apoptosis Detection Kits (Catalogue #C1062S, Beyotime, China). The digested cells were inoculated on a six-well plate at a density of  $2 \times 10^5$  cells/well, and they were allowed to settle overnight to be adherent. Different treatments including (1) growth medium (no treatments, as control), (2) AMG510, (3) HA-TPP, (4) AMG510+HA-TPP, (5) HA-TPP/A were allowed to incubate for 24 h. Cells were then collected and treated with Annexin V-FITC binding buffer and 5  $\mu\text{L}$  of Annexin-V and 10  $\mu\text{L}$  of PI dye for 15 min at room temperature in the dark. Next, the samples measured by flow cytometry. Finally, data were analyzed via FlowJo software.

### 2.16. Western blotting

The Proteins were extracted from cells using RIPA lysis buffers containing protease and phosphatase inhibitors. Protein quantification

was performed using the BCA Protein Quantification Kit (Thermo Fisher Scientific, USA). The equal amount of protein was separated on 8 %–13.5 % tris-glycine gel and then transferred to nitrocellulose filter (NC) membranes. The membranes blocked with 5 % skim milk for 1 h at room temperature and then incubated primary antibody overnight at 4 °C. After incubation, the protein bands washed with TBST (TBS supplemented with 1 % tween-20), and then incubated with appropriate secondary antibody conjugated with HRP for 1 h at room temperature. The protein bands washed four times with TBST for 10 min each, and imaged by the imaging system (Clinx Science Instruments, China).

### 2.17. Immunofluorescence

Cells were grown in coverslips, after treatments the cells were washed three times with PBS for 3 min each, and fixed with 4 % paraformaldehyde for 15 min at room temperature. The coverslips were washed three times with PBS for 3 min each and permeabilized with 0.3 % TritonX-100 in PBS for 15 min, and then blocked with 5 % BSA in PBS for 1 h. Subsequently, cells were incubated with primary antibody overnight at 4 °C, washed three times with PBST (PBS supplemented with 1 % tween-20) for 3 min each and incubated with corresponding secondary antibody in the dark for 2 h at room temperature. After incubation, the cells washed three times with PBST for 3 min each and counterstained by DAPI at room temperature in the dark for 10 min. DAPI was then washed with PBST and imaged by the fluorescence microscopy.

### 2.18. Real-time quantitative PCR (RT-PCR)

Total RNA was extracted by trizol reagent (Accurate Biology, China), and RNA concentration was determined by NanoDrop. Then 1  $\mu\text{g}$  total RNA was reverse-transcribed into cDNA by Evo M-MLV reverse transcription kit II (Accurate Biology, China). Next, RT-PCR was performed according to SYBR Green Super Mix kit (Roche) instructions. Relative mRNA expression (fold change) was calculated using  $2^{-\Delta\Delta\text{CT}}$  method. Primer sequences used in this study are provided in the [Supplementary Information Table S1](#). Each experiment was conducted independently at least three times.

### 2.19. In vivo animal experiments

$5 \times 10^6$  MIA PaCa-2 cells were injected subcutaneously into the right flank of nude mice with a mixture of 80  $\mu\text{L}$  PBS and 20  $\mu\text{L}$  Matrigel (BD Biosciences). The mice were randomly divided into 5 groups with 5 mice in each group. Drug therapy was initiated when the tumor volume reached about 100  $\text{mm}^3$ . The respective treatments were: Control (PBS), AMG510 (10 mg/kg), HA-TPP (10 mg/kg), A + T: AMG510 (10 mg/kg) plus HA-TPP (10 mg/kg), and HA-TPP/A (AMG510 10 mg/kg; HA-TPP 10 mg/kg). Tumor-bearing nude mice were injected intravenously once every two days for a total of 5 times. The body weight of mice was measured every 2 days while the tumor volume of the mice was manually measured with a caliper until day 16, when all mice were killed and treated for further experiments.

### 2.20. In vivo distribution and tumor accumulation

All mice experiments were approved by the Animal Center of South China University of Technology (2019015) and complied with the Regulations on the Administration of Laboratory Animals of The State Council of the People's Republic of China.  $5 \times 10^6$  MIA PaCa-2 cells in PBS mixed with Matrigel (BD Biosciences) at total 100  $\mu\text{L}$  were injected subcutaneously into the right flank of BALB/c nude mice. When the tumor volume reached approximately 100  $\text{mm}^3$ , HA-TPP/A was injected into MIA PaCa-2 tumor-bearing mice through the tail vein. Mice were imaged with In-Vivo Xtreme (Bruker) at different time points (0, 4, 8, 12, 24, 36, 48, 72 h). The mice were sacrificed 24 h after injection, and the

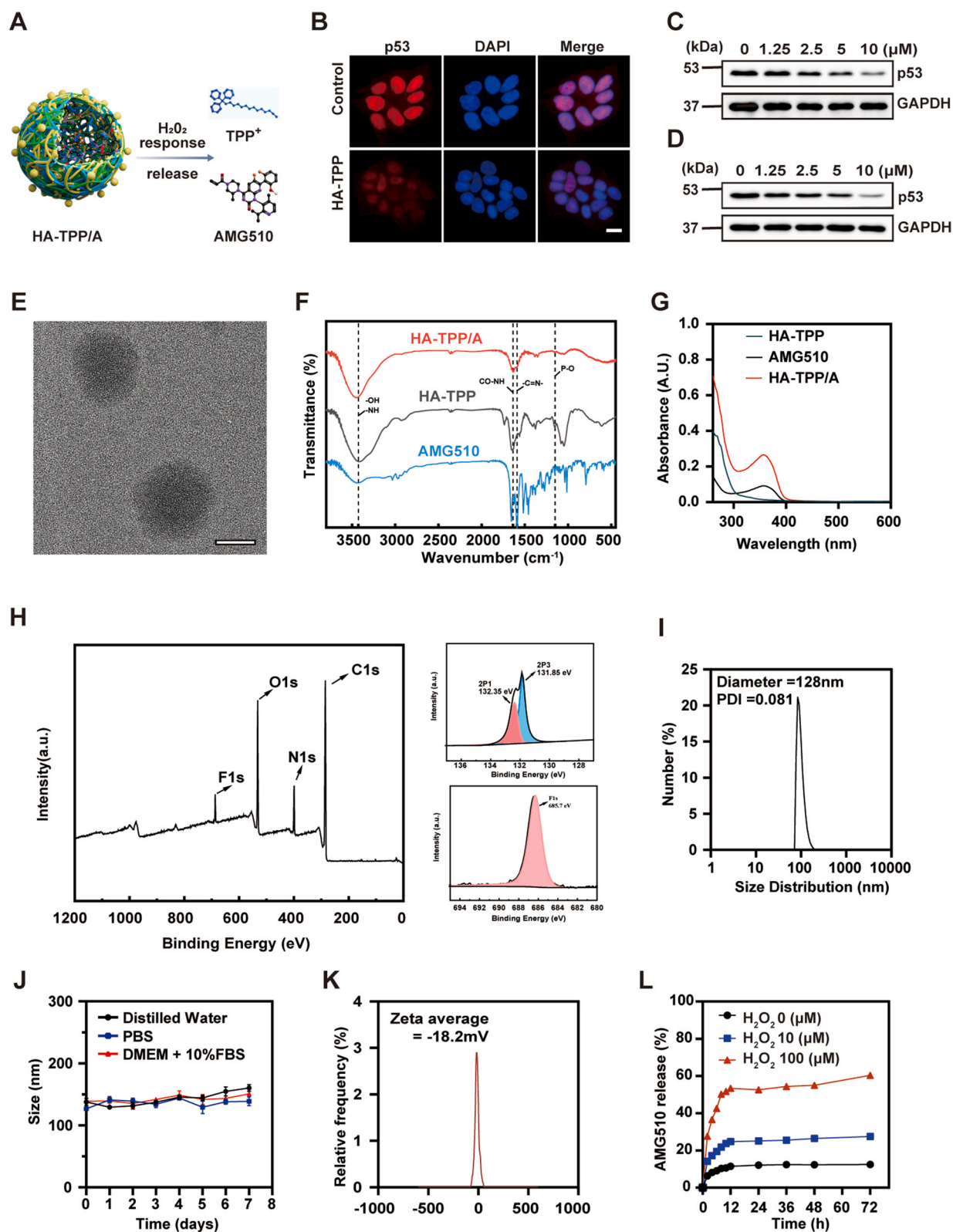


**Fig. 1.** Schematic illustration and characterization of HA-TPP/A nanoparticle. **A)** Schematic illustration of HA-TPP/A nanoparticle. **B)** Fluorescence microscopy images of MIA PaCa-2 cells treated with HA-TPP 5  $\mu$ M for 24 h. Followed by immunostaining with anti-p53 antibody and nucleus staining with DAPI. Scale bar: 20  $\mu$ m. **C)** Western blotting of p53 in MIA PaCa-2 cells and SW837 cells (**D)** after the indicated treatment by different doses of HA-TPP for 24 h. **E)** The TEM images of HA-TPP/A nanoparticle. Scale bars: 100 nm. **F)** FTIR spectra of raw materials and products. **G)** UV-Visible analysis. UV-Visible spectrum of HA-TPP, AMG510 and synthesized HA-TPP/A nanoparticle. **H)** XPS spectrum of HA-TPP/A nanoparticle. **I)** The hydrodynamic size of HA-TPP/A nanoparticle. **J)** Stability of serum proteins of HA-TPP/A nanoparticle. **K)** The zeta potential of HA-TPP/A nanoparticle. **L)** Release profiles of AMG510 from HA-TPP/A nanoparticle in PBS (pH 6.5) after incubation with different concentrations of  $H_2O_2$ . Data are represented as means  $\pm$  SD ( $n = 3$ ).

tumor tissues were harvested, then these organs (heart, liver, spleen, lung, kidney) and tumor were fluorescently imaged with In-Vivo Xtreme.

### 2.21. Toxicity study

After treatment, orbital blood of nude mice was collected and the following indexes were measured by an Automatic Biochemical Analyzer (3100, Hitachi, Japan): ALT, AST, UREA and CRE. Histological changes of the major organs (including heart, liver, spleen, lung, kidney, etc.) of the treated mice were analyzed. The major organs were fixed with 4 % paraformaldehyde, embedded in paraffin, sliced into 5  $\mu\text{m}$  sections and stained with H&E.

### 2.22. Immunohistochemistry

For the immunohistochemistry assays, the tumor was excised and fixed in 4 % paraformaldehyde, embedded in paraffin, and sectioned. Paraffin-embedded tissue sections were dewaxed by xylene and dehydrated by graded ethanol. The cells were incubated with anti-p53 antibody and p-ERK, and the nuclei were stained with hematoxylin. Immunohistochemical images of p53 and p-ERK were captured in Nikon Ti microscope.

### 2.23. Statistical analysis

All experiments were performed in triplicate, the obtained data were analyzed using GraphPad Prism (version 8.0) software and show as the mean  $\pm$  standard deviation (SD). The results from all experiments were analyzed statistically by the two-tailed Student's t-test, where \* $p < 0.05$ , \*\* $p < 0.01$ , \*\*\* $p < 0.001$  and \*\*\*\* $p < 0.0001$  were reflected as statistically significant.

## 3. Results and discussion

### 3.1. Preparation and characterization of HA-TPP/A

HA-TPP was synthesized using a combination of HA, DBCO-NH<sub>2</sub>, oxalyl chloride, and (12-(2-(3-azidopropoxy)-2-oxoacetoxy)-dodecyl)-TPP (Fig. 1A, Scheme S1). The successful synthesis of HA-TPP was confirmed by <sup>1</sup>H NMR, <sup>13</sup>C NMR and MS of the reaction intermediates and the HA-TPP compound, as depicted in Figs. S1–7. We tested the ability of HA-TPP compound to degrade mutp53 protein. Immunofluorescence staining has shown that HA-TPP treatment reduced mutp53 protein levels in MIA PaCa-2 cells (p53<sup>R248W</sup>), revealing diminished fluorescence throughout the cell and particularly in the nucleus (Fig. 1B, Fig. S8). Consistent with this result, western blotting showed that HA-TPP significantly reduced mutp53 levels and these reduction effects were dose-dependent, with significant degradation starting to be observed at 1.25  $\mu\text{M}$  and near-maximal degradation at 10  $\mu\text{M}$  for 24 h treatment in MIA PaCa-2 cells (p53<sup>R248W</sup>) (Fig. 1C). Similar results were obtained in the SW837 cells (p53<sup>R248W</sup>) (Fig. 1D). Subsequently, we further explored whether the combination of HA-TPP, after clearing mutated p53 protein in tumor cells, with the first KRAS inhibitor AMG510 could have a synergistic killing effect on KRAS/TP53 co-mutated digestive tract tumor cells. As shown in Fig. S9, in MIA PaCa-2 (KRAS<sup>G12C</sup>/TP53<sup>R248W</sup>) cells, when the concentration of HA-TPP was fixed at 2.5  $\mu\text{M}$ , it had a significant synergistic killing effect with the concentration of AMG510 at 12.5 nM, 25 nM and 50 nM. Consistent with this result, a fixed concentration of AMG510 also had a significant synergistic killing effect with the different concentration of HA-TPP (Fig. S10) for MIA PaCa-2 cells. Therefore, the molar ratio of TPP: AMG510 was determined to be 100:1 based on cytotoxicity results obtained from MIA PaCa-2 cells. Notably, this ratio can be easily adjusted as per the specific requirements. Whereupon, the HA-TPP/A nanoparticles were prepared using a single-step emulsification method.

Morphology of HA-TPP/A was examined using TEM (Fig. 1E) and SEM (Fig. S11), which indicated that the nanoparticles have a relatively homogeneous spheroid shape. The chemical structure of the HA-TPP/A nanoparticles further verified by the FTIR spectrum (Fig. 1F). The characteristic peaks of AMG510 appear at 1578  $\text{cm}^{-1}$ , which is attributed to C=N stretching vibration. The characteristic peaks of TPP appear at 1150  $\text{cm}^{-1}$ , which is attributed to P-O stretching vibration. Also appearing of a characteristic peak in 1643  $\text{cm}^{-1}$  to HA-TPP attributed to CO-NH amidation reaction. Another distinctive signal appeared at 3445  $\text{cm}^{-1}$  related to the bending vibration of -NH<sub>2</sub> and OH groups to the HA. All characteristic bands of HA-TPP/A at 1578, 1150, 1643, 3445  $\text{cm}^{-1}$  represent the stretching vibration of C=N, P-O, CO-NH bonds, and the bending vibration of NH and OH, respectively, appeared in the AMG510 and HA-TPP spectrum that demonstrated the presence of AMG510 and TPP into HA-TPP/A. The thermal behavior of HA-TPP/A was assessed and the results presented in Fig. S12. According to the results, a significant weight loss of 55% for raw HA-TPP/A was observed in the temperature range of 204°C–463 °C, indicating the decomposition of the HA-TPP matrix. A weight loss of ~25 % in the temperature range of 450°C–573 °C is mainly attributed to the AMG510 and DBCO benzene decomposition. The TGA curve of HA-TPP/A showed ~11 % weight loss from 40 to 110 °C, assigning to the evaporation of adsorbed water. The UV Absorption Spectra confirmed the successful loading of AMG510 by HA-TPP (Fig. 1G). The peak wavelengths of TPP and AMG510 were approximately 270 nm and 350 nm (or 260 nm) respectively, and the HA-TPP/A exhibited two absorption peaks at 260 nm and 245 nm, which indicating the AMG510 was effectively wrapped in HA-TPP. We used UV absorption spectra to evaluate the concentrations of HA-TPP/A. AMG510 and HA-TPP concentrations were calculated according to the standard curve (Figs. S13 and S14). The concentration of HA-TPP was 1.25 mg/mL in HA-TPP sample, and AMG510 was 12.5  $\mu\text{g}/\text{mL}$  in AMG510 sample. The concentrations of HA-TPP and AMG510 were 2.16 mg/mL and 38.42  $\mu\text{g}/\text{mL}$  in HA-TPP/A sample, respectively. The red shift phenomenon could be attributed to the molecular formulation change after self-assembling process. The encapsulation efficiency (EE of AMG510) was 80 % (Table S2). The XPS analyses performed and indicated that the spectrum is dominated by HA-TPP/A excitations arising from carbon, oxygen, oxygen, nitrogen, fluorine (AMG510) and phosphorus (TPP) (Fig. 1H). The hydrodynamic diameter of the HA-TPP/A nanoparticles was determined to be 128 nm, with a PDI value of 0.08, using dynamic light scattering (DLS) on the Anton Paar Litesizer 500 Particle Analyzer (Anton Paar Corporation, Austria) (Fig. 1I, Table S2). The dimensional stability of the nanoparticles in different buffers was evaluated by monitoring their diameter for a week, and no significant differences were observed (Fig. 1J). The zeta potential of the HA-TPP/A nanoparticles was negative, as determined by the Anton Paar Litesizer 500 Particle Analyzer (Fig. 1K, Table S2). Furthermore, the ability of the HA-TPP/A nanoparticles to release AMG510 in response to changes in the ROS level was evaluated. The results showed that an increase in the hydrogen peroxide (H<sub>2</sub>O<sub>2</sub>) level led to a concomitant rise in the release rate of AMG510 (Fig. 1L). This observation was attributed to the ROS-triggered breakage of the diester oxalate bond. Taken together, these results suggested that the HA-TPP/A nanoparticles were successfully synthesized and modified, and are suitable for further investigation as a targeted drug delivery system.

### 3.2. Targeting mitochondria induced mitochondrial damage to degrade mutp53 proteins by HA-TPP/A

The mutp53 protein is known to exhibit oxidative stress as a typical GOF phenotype. Our previous studies have revealed that the cellular redox homeostatic state plays a crucial role in the stability of mutp53, and a high GSH:GSSG ratio stabilizes mutp53 [33]. Since mitochondria are major players in the production and clearance of ROS, damaged mitochondria lead to a large accumulation of intracellular ROS and

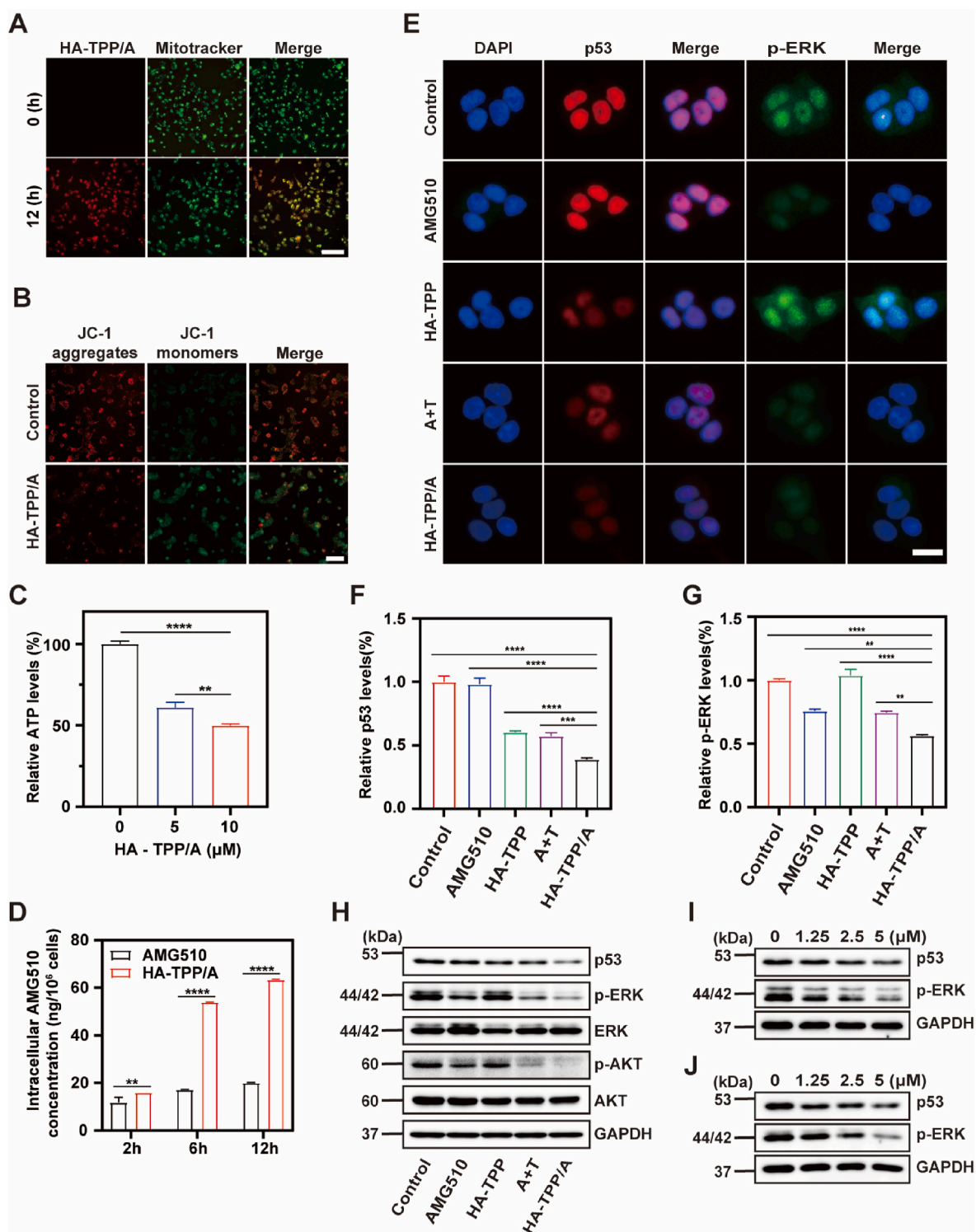


**Fig. 2.** Targeting mitochondria induced mitochondrial damage to degrade mutp53 by treatment with HA-TPP/A. **A)** Fluorescence microscopy images of MIA PaCa-2 cells treated with HA-TPP/A 5 μM (AMG510 50 nM; HA-TPP 5 μM) for 0 h or 12 h and then stained for mitochondria (green, mitotracker). Scale bar: 100 μm. **B)** MMP was measured by JC-1 under a fluorescence microscopy and representative images are displayed. Scale bar: 50 μm. **C)** MIA PaCa-2 cells were treated with different concentrations of HA-TPP/A, and ATP levels were detected using a firefly luciferase-based ATP assay kit. Data are represented as means ± SD (n = 3). **D)** Intracellular AMG510 concentration of MIA PaCa-2 cells after incubation with various groups at 2, 6 or 12 h. **E)** Fluorescence microscopy images of SW837 cells after the indicated treatment for 24 h. Dosing: AMG510 (50 nM), HA-TPP (5 μM), A + T (AMG510 50 nM plus HA-TPP 5 μM), HA-TPP/A (5 μM). Followed by immunostaining with anti-p53 antibody, anti-p-ERK antibody and nucleus staining with DAPI. Scale bar: 20 μm. **F)** Quantified results of p53 and p-ERK (**G**) levels. Data are represented as means ± SD (n = 3). **H)** Western blotting of p53, p-ERK and p-AKT proteins in SW837 cells after the indicated treatment for 24 h. Dosing: AMG510 (50 nM), HA-TPP (5 μM), A + T (AMG510 50 nM plus HA-TPP 5 μM), HA-TPP/A (5 μM). **I)** Western blotting of p53 and p-ERK in MIA PaCa-2 cells after the indicated treatment by different doses of HA-TPP/A for 24 h. **J)** Western blotting of p53 and p-ERK in SW837 cells after the indicated treatment by different doses of HA-TPP/A for 24 h. (\*\*p < 0.01, \*\*\*p < 0.001 and \*\*\*\*p < 0.0001).

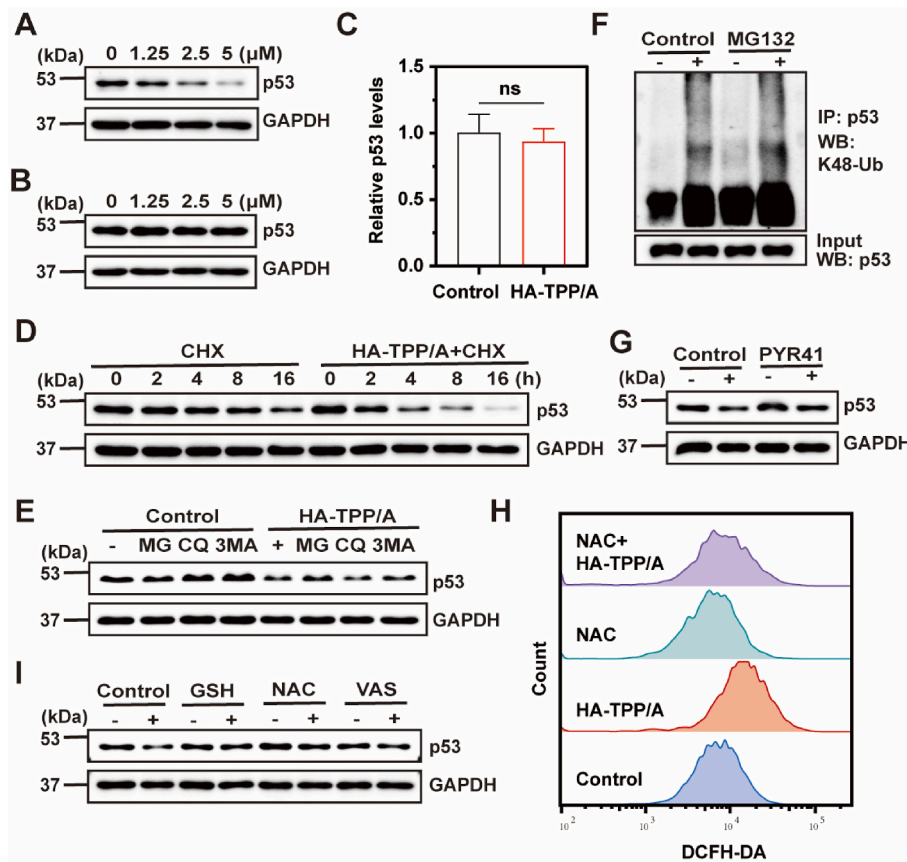


**Fig. 3.** HA-TPP/A elicited ubiquitination-dependent proteasomal degradation of mutp53. A) Western blotting of p53 in DLD-1 ( $p53^{S241F}$ ) cells after the indicated treatment by different doses of HA-TPP/A for 24 h. B) Western blotting of p53 in T84 ( $wtp53$ ) cells after the indicated treatment by different doses of HA-TPP/A for 24 h. C) Relative p53 mRNA level in SW837 cells treated with or without HA-TPP/A (5  $\mu$ M) for 24 h, analyzed by RT-PCR. The values of the HA-TPP/A group were normalized against those of the control group. Data are represented as means  $\pm$  SD ( $n = 3$ ) (ns: no significance). D) Western blotting of p53 in MIA PaCa-2 cells treated with cycloheximide (CHX, 20  $\mu$ M) either in the absence or presence of HA-TPP/A (5  $\mu$ M). E) Western blotting of p53 in SW837 cells after the indicated treatment for 24 h. Dosing: HA-TPP/A, 5  $\mu$ M; MG132, 5  $\mu$ M; CQ, 50  $\mu$ M; 3MA, 50 mM. F) Whole cell extract was immunoprecipitated with anti-p53 antibody and then immunoblotted with anti-K48-Ub antibody. The lower panel showed the Western blotting of p53 in SW837 cells. G) Western blotting of p53 in SW837 cells after the indicated treatment for 24 h. Dosing: HA-TPP/A, 5  $\mu$ M; PYR41, 5  $\mu$ M. H) Flow cytometric analysis for intracellular ROS was detected by DCFH-DA after different treatments for 12 h in MIA PaCa-2 cells. Dosing: HA-TPP/A (5  $\mu$ M); NAC, 500  $\mu$ M. I) Western blotting of p53 in SW837 cells after the indicated treatment for 24 h. Dosing: HA-TPP/A (5  $\mu$ M); GSH, 2 mM; NAC, 500  $\mu$ M; VAS2870 (VAS), 20  $\mu$ M.

eventually cell death. Therefore, we have developed a HA-TPP/A nanoparticle that can target mitochondria to modulate cellular redox levels. The analysis of fluorescent microscope revealed the co-localization of Cy5.5-HA-TPP/A (red) and mitochondria (green), verifying HA-TPP/A accumulated in mitochondria (Fig. 2A, Fig. S15). While JC-1 staining, a common dye used for assessing mitochondrial membrane potential (MMP), has confirmed that it triggers the loss of mitochondrial integrity, as a significant decrease in fluorescence ratio (red/green) after HA-TPP/A treatment (Fig. 2B). Consistent with this result, HA-TPP/A treatment also decreased the intracellular ATP level (Fig. 2C), suggesting the mitochondrial damage ability of HA-TPP/A nanoparticle. Cell uptake experiment was performed via various treatments (free AMG510 and HA-TPP/A), and the results (Fig. 2D) showed that compared with free AMG510, the content of AMG510 entering cancer cells in NPs was enhanced. By incorporating HA in HA-TPP/A improved the delivery of TPP and AMG510 to tumor cells with rich CD44 receptors.

We have also evaluated the ability of HA-TPP/A nanoparticle to degrade mutp53 protein and inhibit mutant KRAS downstream signaling pathways. Immunofluorescence staining revealed that HA-TPP/A treatment reduced mutp53 protein levels in SW837 cells (KRAS<sup>G12C</sup> and p53<sup>R248W</sup>), revealing diminished fluorescence throughout the cell and particularly in the nucleus (Fig. 2E). This reduction in mutp53

protein level was due to HA-TPP rather than AMG510, as demonstrated by minimal change in mutp53 protein fluorescence after AMG510 treatment (Fig. 2F). Additionally, the key KRAS downstream pathway effector protein *p*-ERK [49] was also decreased by HA-TPP/A or AMG510 treatment (Fig. 2G). Importantly, the reduction effects of mutp53 and *p*-ERK were more pronounced after HA-TPP/A treatment than co-treatment with HA-TPP and AMG510, demonstrating the superiority of the co-delivery system over combined treatment. The superior capacity of NPs to inhibit p53 and *p*-ERK might mainly be related to more AMG510 entering the cells. Consistent with this result, western blotting showed that HA-TPP/A significantly reduced mutp53, *p*-ERK and *p*-AKT levels in the SW837 cell line, and these reduction effects were much better than those observed in the group of two drugs combined treatment (Fig. 2H). The mutp53 and *p*-ERK reducing effect by HA-TPP/A was both dose- and time-dependent, with significant degradation starting to be observed at 1.25  $\mu$ M and near-maximal degradation at 5  $\mu$ M for 24 h treatment in MIA PaCa-2 cells (Fig. 2I, Fig. S16). Similar results were obtained in the SW837 cell line (Fig. 2J, Fig. S17). Taken together, these results suggested that the HA-TPP/A nanoparticle is a promising strategy for the treatment of cancer patients with KRAS mutation and mutp53 protein expression.

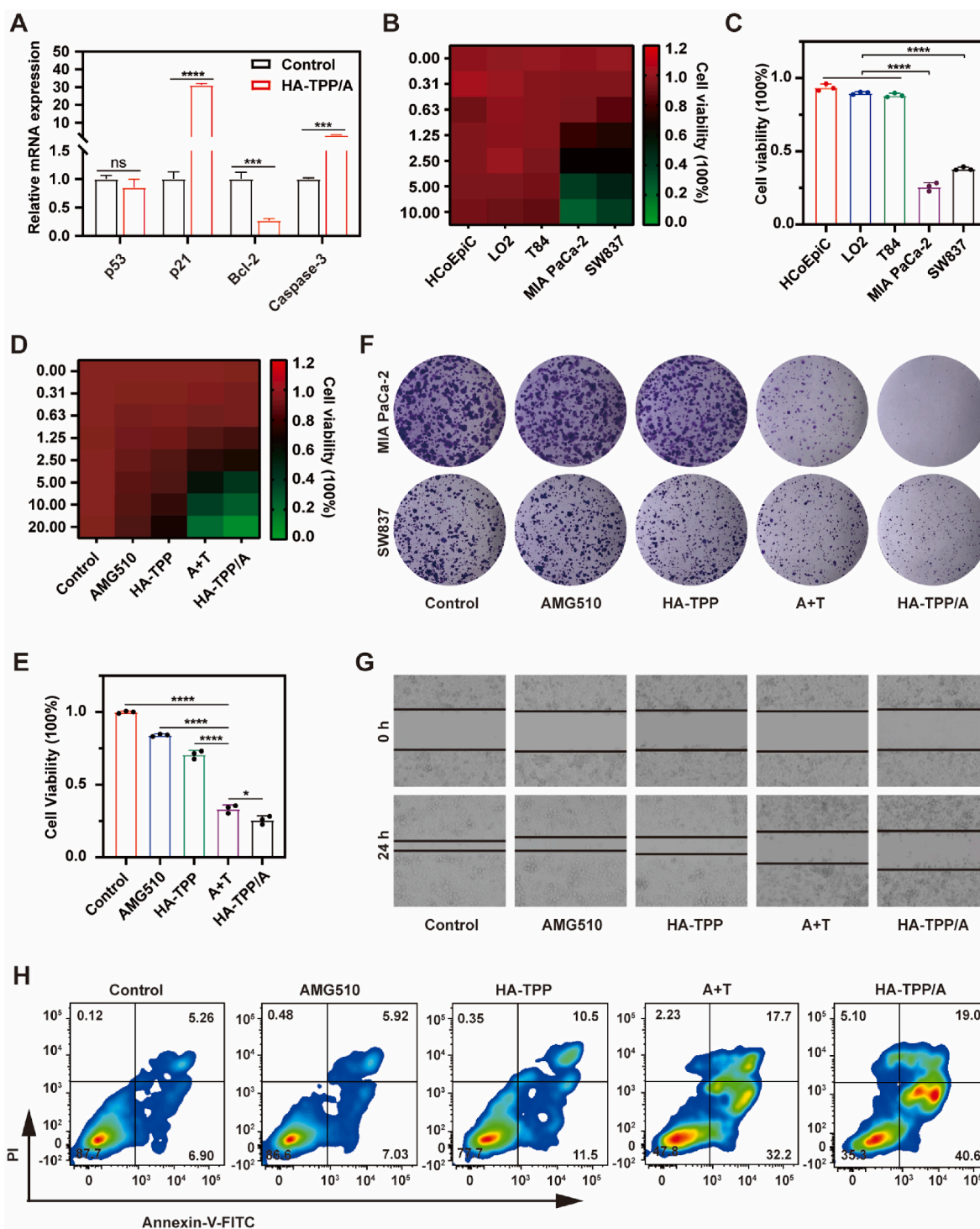


**Fig. 4.** Abrogation of mutp53 protein conferred GOF phenotypes and co-targeting effects in vitro. A) Relative mRNA level of mutp53 downstream pathway in MIA PaCa-2 (p53<sup>R248W</sup>) cells treated with or without HA-TPP/A (5 μM) for 24 h, analyzed by RT-PCR. The values of the HA-TPP/A group were normalized against those of the control group. B) Cytotoxicity tests of the normal intestinal epithelial cells (HCoEpiC), normal hepatocytes (LO2), wtp53 CRC cell (T84), mutp53 cells MIA PaCa-2 (p53<sup>R248W</sup>) and SW837 (p53<sup>R248W</sup>) after the indicated treatment for 24 h by HA-TPP/A. Data are represented as means ± SD (n = 3). C) Cytotoxicity tests after 24 h by treatment of HA-TPP/A 10 μM (AMG510 100 nM; HA-TPP 10 μM) in HCoEpiC, LO2, T84, MIA PaCa-2 and SW837 cells. D) Cell viability on MIA PaCa-2 cells after the indicated treatment for 24 h by AMG510, HA-TPP, A + T (AMG510 plus HA-TPP) and HA-TPP/A. Data are represented as means ± SD (n = 3). E) Viability of MIA PaCa-2 cells after the indicated treatment for 24 h. Dosing: AMG510 (100 nM), HA-TPP (10 μM), A + T (AMG510 100 nM plus HA-TPP 10 μM), HA-TPP/A (10 μM). F) Clonal formation assay of control MIA PaCa-2 and SW837 cells and after treatment with AMG510, HA-TPP, AMG510+HA-TPP, HA-TPP/A for 12 d at the indicated condition. Dosing: AMG510 (10 nM), HA-TPP (1 μM), A + T (AMG510 10 nM plus HA-TPP 1 μM), HA-TPP/A 1 μM (AMG510 10 nM; HA-TPP 1 μM). G) Cell migration inhibition of MIA PaCa-2 cells after the indicated treatment for 24 h. Dosing: AMG510 (100 nM), HA-TPP (10 μM), A + T (AMG510 100 nM plus HA-TPP 10 μM), HA-TPP/A (10 μM). Data are represented as means ± SD (n = 3). H) Flow cytometric analysis of cell apoptosis of MIA PaCa-2 cells after different treatments for 24 h. Dosing: AMG510 (100 nM), HA-TPP (10 μM), A + T (AMG510 100 nM plus HA-TPP 10 μM), HA-TPP/A (10 μM). (\*p < 0.05, \*\*\*p < 0.001 and \*\*\*\*p < 0.0001).

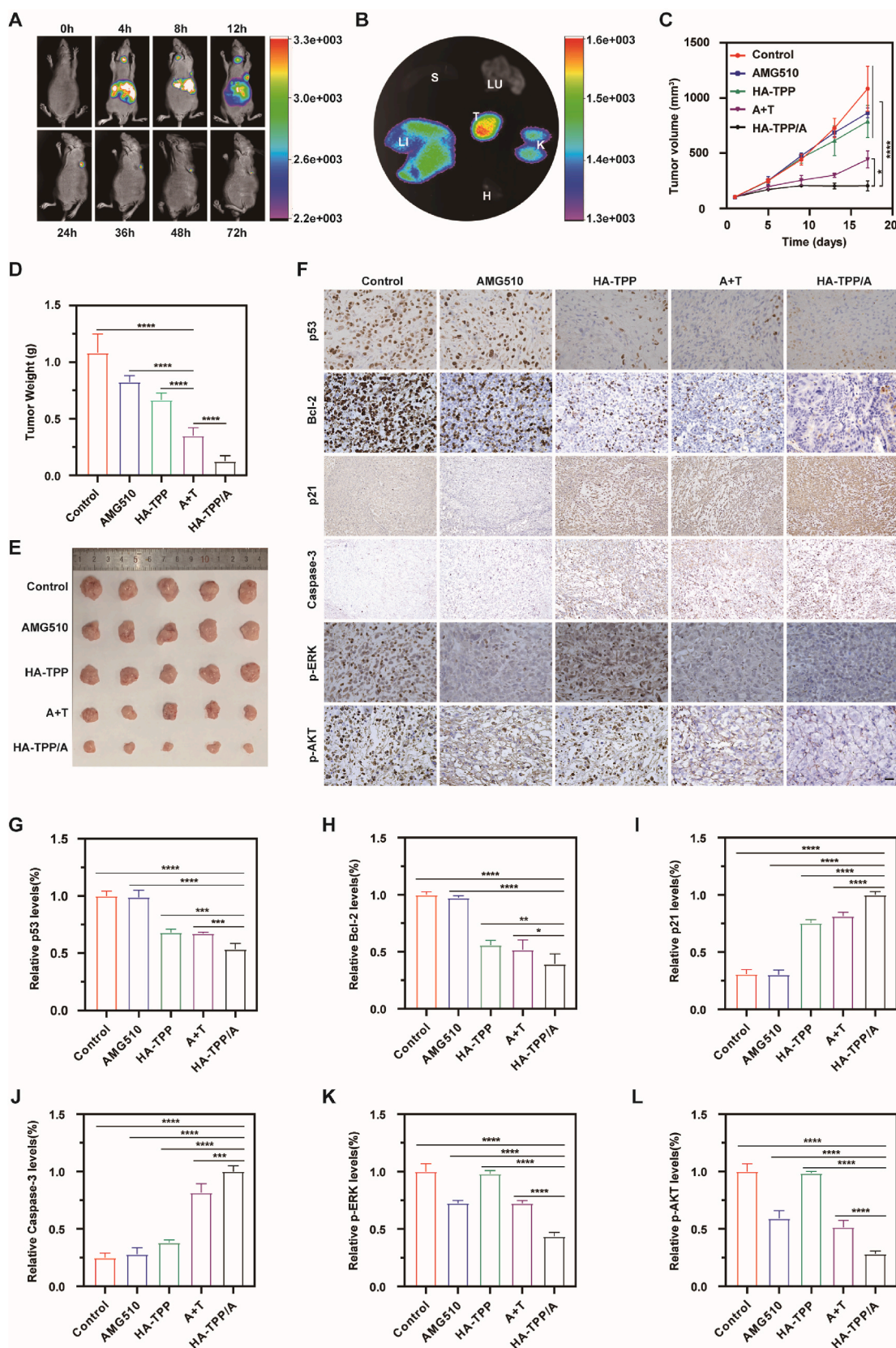


**Fig. 5.** *In vivo* antitumor effects and pathological mechanism of HA-TPP/A. A) *In vivo* fluorescence biodistribution of Cy5.5-labeled HA-TPP/A post-injection in MIA PaCa-2 tumor-bearing nude mice. B) *Ex vivo* fluorescence distribution in tumor and major organs of Cy5.5-labeled HA-TPP/A 24 h post-injection in MIA PaCa-2 tumor-bearing nude mice (H: Heart, LI: Liver, LU: Lung, S: Spleen, LU: Lung, K: Kidney, T: Tumor). C) Tumor-volume curves of nude mice treated with various treatments. D) Tumor-weight and picture of the tumors (E) collected from mice after various treatments. F) Immunohistochemical staining of p53, Bcl-2, p21, Caspase-3, p-ERK and p-AKT of tumors in different groups. Scale bar: 100  $\mu$ m. Data are represented as means  $\pm$  SD (n = 5). G) Quantitative analysis of immunohistochemical staining of p53, Bcl-2 (H), p21 (I), Caspase-3 (J), p-ERK (K) and p-AKT (L) of tumors in different groups. (\*p < 0.05, \*\*p < 0.01, \*\*\*p < 0.001 and \*\*\*\*p < 0.0001).

### 3.3. HA-TPP/A elicited ubiquitination-dependent proteasomal degradation of mutp53

To further understand the molecular mechanism of the decrease of mutp53 caused by HA-TPP/A. We first assessed the potential mutp53-targeting effect of HA-TPP/A to degrade different mutp53. We conducted western blotting in the CRC DLD-1 and PDAC PATU-8988S cells, which harbored S241F and R282W mutation in the *TP53* gene, respectively. HA-TPP/A significantly reduced mutp53 level in DLD-1 cells (Fig. 3A) and PATU-8988S cells (Fig. S18). These findings indicate that HA-TPP/A has the capacity to induce wide-spectrum degradation, to the various extent, in different hot-spot mutations p53. In contrast to mutp53, the level of wtp53 protein in the two CRC cell lines we tested, T84 (Fig. 3B) and HCT8 (Fig. S19), were not affected by HA-TPP/A, indicating that HA-TPP/A induced selective degradation of mutp53. To understand how HA-TPP/A elicit mutp53 degradation, we performed RT-PCR to determine whether the decrease in mutp53 levels was in response to downregulated *TP53* expression in these cells. The result showed that HA-TPP/A did not alter transcription of the mutated *TP53* gene (Fig. 3C). Further investigations revealed that HA-TPP/A enhanced the depletion of p53<sup>R248W</sup> (Fig. 3D, Fig. S20), resulting in post-transcriptional mutp53 depletion. We examined two major protein-degradation pathways in eukaryotic cells, the ubiquitin-proteasome system (UPS) and autophagy-lysosome pathway (ALP) [50,51], and found that the ALP was not mediated in HA-TPP/A-induced mutp53 degradation. In contrast, the UPS pathway was critical in the HA-TPP/A-induced degradation of mutp53, as treatment with MG132 completely abrogated the mutp53-degrading activity of HA-TPP/A in SW837 cells (Fig. 3E). Similar results were obtained in the MIA PaCa-2 cells (Fig. S21). Furthermore, ubiquitination of mutp53 proteins were increased by HA-TPP/A treatment, and a further enhance in ubiquitinated mutp53 protein levels induced by MG132 (Fig. 3F, Fig. S22). PYR41, a protein ubiquitination inhibitor [52], reversed the mutp53-degrading activity of HA-TPP/A (Fig. 3G, Fig. S23). Therefore, our results indicated that HA-TPP/A can target and damage mitochondria, leading to the degradation of mutp53 proteins via the UPS pathway. In order to further burrow into the molecular mechanism of HA-TPP/A inducing mutp53 degradation, we evaluated the possible role of ROS. Intracellular ROS was detected by DCFH-DA probes and analyzed by flow cytometry (Fig. 3H, Fig. S24). The results showed that the level of intracellular ROS of HA-TPP/A-treated MIA PaCa-2 cells was markedly increased, while intracellular ROS decreased significantly after treatment with ROS inhibitors (GSH, NAC and VAS), which suggested that the level of intracellular ROS increase mediated by HA-TPP is reversible. To further explore whether ROS increase abnormally affects p53 expression. HA-TPP/A was co-treated with various ROS inhibitors, and the results showed that all these inhibitors could inhibit the degradation of mutp53 induced by HA-TPP/A (Fig. 3I, Fig. S25), indicating that HA-TPP/A elicited degradation of mutp53 dependent on targeting mitochondria damage induced disorder of intracellular redox equilibrium.

### 3.4. Abrogation of mutp53 protein conferred GOF phenotypes and dual-targeting effects in vitro

In addition to inhibition of wtp53 activities by mutp53, compelling evidence demonstrates that mutp53 proteins have novel GOF activities that contribute to tumorigenesis and metastasis [53]. One mechanism of mutp53 GOF involves the interaction with other transcription factors to upregulate genes promoting tumorigenesis, metastasis, and drug resistance. To validate this, RT-PCR experiments were performed on gastrointestinal cancers cell line to determine the effect of HA-TPP/A-mediated mutp53 degradation on downstream transcription factors including the apoptosis-regulating family genes *Bcl-2* [54], *p21* and *Caspase-3* [55]. The results indicated that HA-TPP/A treatment reduced *Bcl-2* mRNA expression, and increased *p21* and *Caspase-3*

mRNA expression in MIA PaCa-2 (p53<sup>R248W</sup>) cells (Fig. 4A). Similar results were obtained in SW837 (p53<sup>R248W</sup>) cells (Fig. S26). These results suggesting that the GOF effect of mutp53 was abolished by the degradation of mutp53. Further experiments revealed that HA-TPP/A treatment exhibited specific killing effects on p53 mutant cells, including MIA PaCa-2 (p53<sup>R248W</sup>) and SW837 (p53<sup>R248W</sup>), while having only weak effects on wtp53 CRC cells T84, normal intestinal epithelial cells HCoEpiC, and normal hepatocytes LO2 (Fig. 4B and C). Considering the co-alteration of *KRAS-TP53* predicts a poor prognosis and triggers metastasis in CRC patients, novel bi-target therapeutic strategies are necessary to treat co-mutations and evaluate anti-proliferation and anti-metastasis activities. In an MTT assay, all drug formulations showed concentration dependent cytotoxicity in MIA PaCa-2 (Fig. 4D) and SW837 (Fig. S27), while combined drug formulations of HA-TPP and AMG510 exhibited enhanced cytotoxicity, demonstrating strong synergistic effects in killing MIA PaCa-2 (Fig. 4E) and SW837 cells (Fig. S28). Based on the preliminary cytotoxicity results of HA-TPP and AMG510, the most obvious synergistic killing effect of the ratio of HA-TPP:AMG510 was 100:1. Next, we calculated the combination index by Compusyn to vary the concentrations of HA-TPP and AMG510 used in the two-drug combinations. Ratio validation using viability assays of two-drug at HA-TPP and AMG510 were performed in MIA PaCa-2 cells to confirm that the selected ratios were synergistic. And the results (Fig. S29) showed that between HA-TPP and AMG510 has the synergistic effects. In addition, HA-TPP/A nanoparticles showed higher cytotoxicity, possibly due to increased drug uptake via endocytosis in gastrointestinal cancer cells. Consistent with this result, a colony formation assay demonstrated that AMG510 and HA-TPP combined treatment reduced colony formation compare with the single drug treatment with either of the two drugs, and a higher reduction in the group of the HA-TPP/A nanoparticle (Fig. 4F). To evaluate the anti-migration effects of various drug formulations, a wound healing assay was performed. As shown in Fig. 4G, various drug formulations showed different degrees of inhibition in MIA PaCa-2 cells. Compared with single drug groups, combined drug group exhibited stronger antimigration efficiency, indicating that the co-altered *KRAS-TP53* might play a vital role in gastrointestinal tumor migration and the combination therapy enhanced inhibition of tumor cells migration. Compared with HA-TPP and AMG510 combined treatment group, the results in the co-loaded HA-TPP/A nanoparticles showed larger wound width, resulting in tumor cell migration inhibition, in a manner consistent with cytotoxicity assays. Next, the therapeutic effects of different treatment groups were analyzed through flow cytometry. As shown in the apoptosis chart (Fig. 4H), compared with the control group, the apoptosis rate of HA-TPP/A reached the highest level of 59.6 %, which was about 4.6 times and 2.7 times that of the free AMG510 and HA-TPP group. These results suggest that a double targeting therapy for *KRAS-TP53* co-mutation will be essential, as a one-p53-drug-fits-all approach is bound to fail [56]. Therefore, combination therapy may simultaneously suppress the proliferation, migration and promote apoptosis of tumor cells with co-altered *KRAS-TP53*.

### 3.5. HA-TPP/A dual-targeting oncogenic mutant *KRAS* and mutp53 inhibited tumor growth in vivo

The *in vivo* and *ex vivo* fluorescence biodistribution of Cy5.5-HA-TPP/A on MIA PaCa-2 tumor-bearing mice. And the tumoral fluorescence intensity gradually increased from 8 h and well maintained up to 72 h after by tail vein injections (Fig. 5A). The *ex vivo* images, including the excised major organs (heart, liver, spleen, lung and kidney) and tumor of mice, showed that the nanoparticles mainly located in tumor (Fig. 5B), suggesting the good tumor-specific accumulation of HA-TPP/A attributed to an enhanced permeability and retention (EPR) [57] effect and HA-CD44 recognition in tumor sites [58–60]. Based on the *in vivo* distribution results, HA-TPP/A was achieved effective enrichment in tumor areas. Finally, the tumor inhibition ability of HA-TPP/A *in vivo*

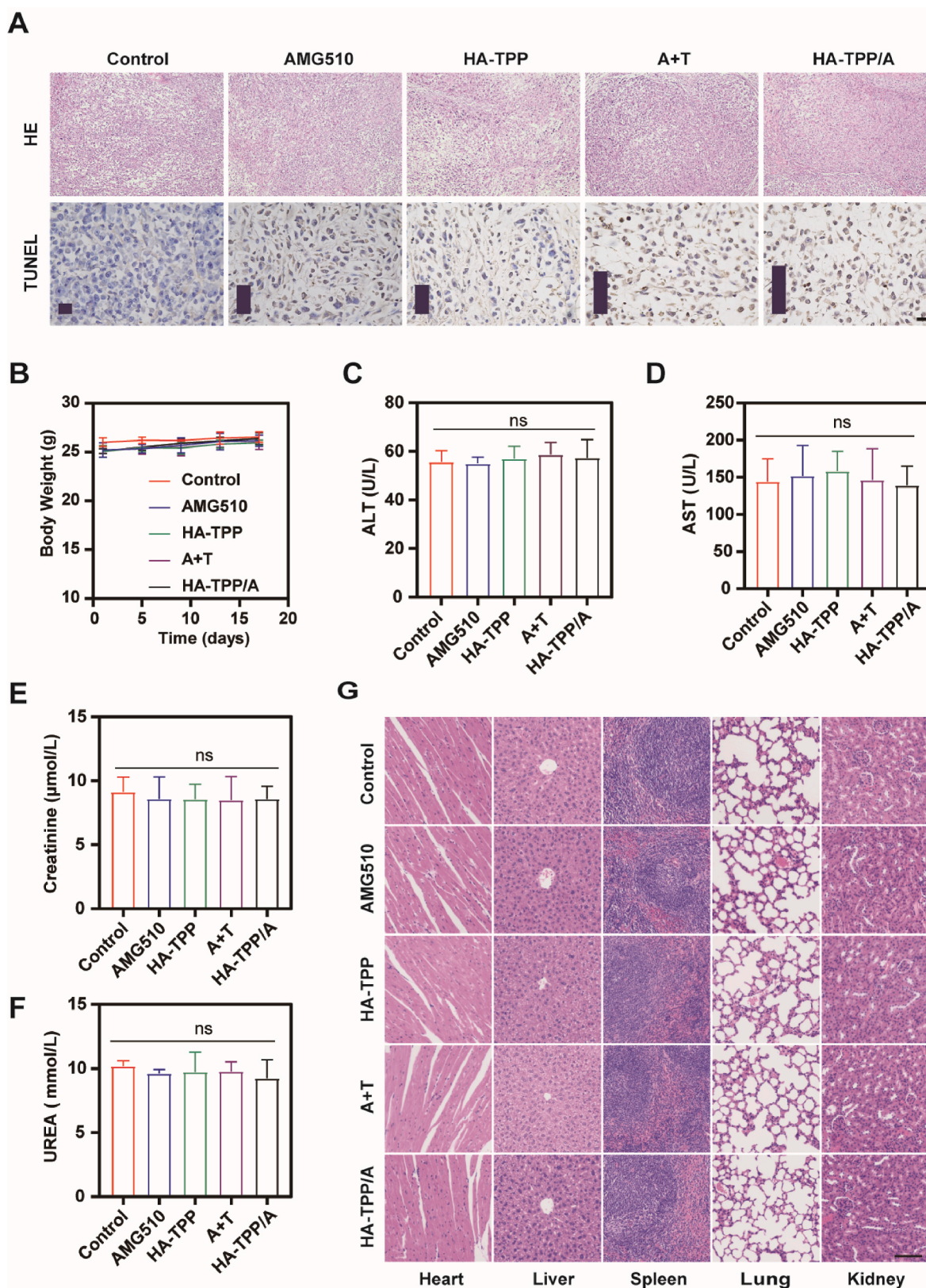


**Fig. 6.** *In vivo* biological safety assessment of HA-TPP/A. A) H&E staining and TUNEL analysis of tumors in different groups. Scale bar: 100  $\mu\text{m}$ . B) Body-weight curves of nude mice treated with various treatments. C) Serum ALT, AST (D), CRE (E) and UREA (F) tested of nude mice received different treatments. G) H&E staining in major organs of mice receiving different treatments. Scale bar: 100  $\mu\text{m}$ . Data are represented as means  $\pm$  SD (n = 5).

was investigated. When the tumor volume grew to about 100 mm<sup>3</sup>, MIA PaCa-2 tumor-bearing mice were randomly divided into five groups. The respective treatments were: Control (PBS), AMG510 (10 mg/kg), HA-TPP (10 mg/kg), A + T: AMG510 (10 mg/kg) plus HA-TPP (10 mg/kg), and HA-TPP/A (AMG510 10 mg/kg; HA-TPP 10 mg/kg). Tumor-bearing nude mice were injected intravenously once every two days for a total of 5 times. The tumor volumes in various treatment groups were recorded every 2 days. On day 16 post-treatment, either the group of AMG510 or HA-TPP monotherapy regimens showed a mild tumor suppression efficacy compared with the control group. By comparison, AMG510 and HA-TPP combination therapy greatly improved the treatment outcome, substantiating the synergistic antitumor effect. Besides, the group of the HA-TPP/A group had the best tumor growth inhibition ability, indicating the excellent antitumor effect (Fig. 5C), as revealed by excised tumor weight (Fig. 5D and E). As shown in Fig. 5F, immunohistochemical detection revealed that the expression level of mutp53 protein (Fig. 5G) and Bcl-2 protein (Fig. 5H) were down-regulated, with up-regulated of p21 (Fig. 5I) and Caspase-3 protein (Fig. 5J) within the tumor tissue of mice in these treatment groups containing HA-TPP. The expression level of p-ERK protein (Fig. 5K) and p-AKT protein (Fig. 5L) were down-regulated within the tumor tissue of mice in these treatment groups containing AMG510. These results indicated that HA-TPP/A nanoparticles have powerful tumor targeting drug delivery capabilities and contribute to reinforcing the combination effects on inhibiting tumor growth *in vivo* of tumor-bearing mice. KRAS and TP53 are the "star molecules" in tumor genes, and RAS and p53 proteins are two "unpharmaceutical" "notorious" targets. There is increasing evidence that simultaneous mutation of p53 and KRAS proteins has synergistic cancer-promoting consequences. For example, mutant p53 can increase KRAS activity in pancreatic cancer by regulating RNA splicing [61]. KRAS mutants activate a transcription factor called CREB1, which can directly interact with mutant p53, resulting in abnormal expression of multiple genes [62]. The up-regulation of FOXA1, a transcription factor that promotes cancer metastasis, activates the Wnt/ $\beta$ -catenin signaling pathway and promotes tumor metastasis. Although the specific regulatory relationship between KRAS and p53 is still unclear, combined with existing studies, our investigated the potential of a mitochondria-targeted functionalized nano-carrier HA-TPP to co-deliver AMG510 as the double targeting therapeutic strategy, by inhibiting the mutant KRAS and mutp53 signaling pathways providing a promising approach for therapy in highly malignant tumors with KRAS-TP53 co-mutation and potentially expanding clinical indications for AMG510 targeted therapies in gastrointestinal tumors.

### 3.6. Biosafety evaluation of HA-TPP/A *in vivo*

Consistent with the therapeutic efficacy of HA-TPP/A, TUNEL staining and quantities of the apoptotic cells by square patterns demonstrated that apoptosis was lesser elevated in the group of AMG510 or HA-TPP, AMG510 and HA-TPP combination therapy greatly increased apoptosis in the cells within the tumor tissue (Fig. 6A). To further evaluate the biological safety of HA-TPP/A, the mice body weight in all groups shows no significant change after 16 days treatment, indicating no severe acute toxicity of HA-TPP/A (Fig. 6B). The H&E analysis of major organs (heart, liver, spleen, lung and kidney) and blood biochemical indexes analysis, including serum aminotransferase (ALT), aspartate aminotransferase (AST), creatinine (CRE), and blood urea nitrogen (UREA) were also performed after the treatment course. There were no significantly blood biochemical indexes abnormal (Fig. 6C–F) and pathological change in major organs of mice receiving different treatments (Fig. 6G). These results indicated that HA-TPP/A nanoparticles displayed a good biosafety profile and thus gained a preliminary indication for the potential clinical translation.

## 4. Conclusion

In summary, we reported on the development of a novel nano-material, HA-TPP/A, capable of inducing apoptosis in tumor cells through mitochondrial damage and disruption of intracellular redox equilibrium, resulting in the degradation of mutp53 proteins via the UPS pathway. Notably, this is the first reported KRAS-TP53 co-mutation systematic nanomaterial that exhibits potent targeting ability against highly malignant gastrointestinal tumors. These findings demonstrate the potential clinical applications of HA-TPP/A in the treatment of KRAS-TP53 comutant tumors and suggest a new avenue for the use of AMG510 targeted therapies in gastrointestinal tumors.

Admittedly, as the world's first FDA-approved tumor therapy drug targeting KRAS mutation, AMG510 is currently only used in adult patients with KRASG12C mutation. However, KRAS has multiple site mutations, resulting in limited clinical application of AMG510. Therefore, the major limitation of HA-TPP/A nanoparticles is also only for the tumors with TP53 and KRASG12C co-mutations. What also deserves expecting is that HA-TPP/A-mediated degradation of mutant p53 has the potential to recoup the current defects in mutant KRAS treatment, and this is also our future research.

### Ethics approval

All animal experiments were approved by Animal Center of South China University of Technology (2019015) and were performed in compliance with the Regulation on the Administration of Laboratory Animals established by the State Council, the People's Republic of China.

### CRedit authorship contribution statement

**Yong Mei:** Investigation, Methodology, Data curation, Writing – original draft. **Xiaohua Qin:** Methodology, Data curation, Writing. **Zhenyu Yang:** Investigation, Methodology. **Shiyao Song:** Methodology, Data curation. **Xiaoting Liu:** Data curation. **Chong Wu:** Data curation. **Jieying Qian:** Data curation. **Xiaowan Huang:** Data curation. **Yunjiao Zhang:** Conceptualization, Writing – review & editing, Resources, Supervision, Project administration. **Weiling He:** Conceptualization, Writing – review & editing, Resources, Supervision, Funding acquisition, Project administration.

### Declaration of competing interest

All authors declared no competing interests.

### Acknowledgments

This work was supported by the National Key Research and Development Plan (2022YFC3401000), National Natural Science Foundation of China (81871994, 82022037, T2222014 and 32071398), Guangdong Provincial Natural Science Foundation (2019B151502063), Guangdong Basic and Applied Basic Research Foundation (2021B1515230009), Key Research and Development Plan of Guangdong Province (2020B0101030006, 2020B1515120096 and 2022B0202010002).

### Appendix A. Supplementary data

Supplementary data to this article can be found online at <https://doi.org/10.1016/j.bioactmat.2023.10.003>.

### References

- [1] J. Huang, D.E. Lucero-Prisco 3rd, L. Zhang, W. Xu, S.H. Wong, S.C. Ng, M.C. S. Wong, Updated epidemiology of gastrointestinal cancers in East Asia, *Nat. Rev. Gastroenterol. Hepatol.* 20 (2023) 271–287, <https://doi.org/10.1038/s41575-022-00726-3>.

- [2] A. Grothey, M. Fakih, J. Tabernero, Management of BRAF-mutant metastatic colorectal cancer: a review of treatment options and evidence-based guidelines, *Ann. Oncol.* 32 (2021) 959–967, <https://doi.org/10.1016/j.annonc.2021.03.206>.
- [3] J. Wu, X. Wang, L. Chen, J. Wang, J. Zhang, J. Tang, Y. Ji, J. Song, L. Wang, Y. Zhao, H. Zhang, T. Li, J. Sheng, D. Chen, Q. Zhang, T. Liang, Oxygen microcapsules improve immune checkpoint blockade by ameliorating hypoxia condition in pancreatic ductal adenocarcinoma, *Bioact. Mater.* 20 (2023) 259–270, <https://doi.org/10.1016/j.bioactmat.2022.05.022>.
- [4] R.L. Siegel, K.D. Miller, H.E. Fuchs, A. Jemal, *Cancer statistics, 2022*, *CA Cancer J Clin* 72 (2022) 7–33, <https://doi.org/10.3322/caac.21708>.
- [5] B. Vogelstein, N. Papadopoulos, V.E. Velculescu, S. Zhou, L.A. Diaz Jr., Kinzler KW, Cancer genome landscapes, *Science* 339 (2013) 1546–1558, <https://doi.org/10.1126/science.1235122>.
- [6] R.G. Amado, M. Wolf, M. Peeters, E. Van Cutsem, S. Siena, D.J. Freeman, T. Juan, R. Sikorski, S. Suggs, R. Radinsky, S.D. Patterson, D.D. Chang, Wild-type KRAS is required for panitumumab efficacy in patients with metastatic colorectal cancer, *J. Clin. Oncol.* 26 (2008) 1626–1634, <https://doi.org/10.1200/jco.2007.14.7116>.
- [7] D.P. Modest, I. Ricard, V. Heinemann, S. Hegewisch-Becker, W. Schmiegel, R. Porschen, S. Stintzing, U. Graeven, D. Arnold, L.F. von Weikersthal, C. Giessen-Jung, A. Stahler, H.J. Schmoll, A. Jung, T. Kirchner, A. Tannapfel, A. Reinacher-Schick, Outcome according to KRAS-, NRAS- and BRAF-mutation as well as KRAS mutation variants: pooled analysis of five randomized trials in metastatic colorectal cancer by the AIO colorectal cancer study group, *Ann. Oncol.* 27 (2016) 1746–1753, <https://doi.org/10.1093/annonc/mdw261>.
- [8] M. Drost, M. Barbacid, Targeting the MAPK pathway in KRAS-driven tumors, *Cancer Cell* 37 (2020) 543–550, <https://doi.org/10.1016/j.ccell.2020.03.013>.
- [9] C.C. Wong, J.L. Wu, F. Ji, W. Kang, X. Bian, H. Chen, L.S. Chan, S.T.Y. Luk, S. Tong, J. Xu, Q. Zhou, D. Liu, H. Su, H. Gou, A.H. Cheung, K.F. To, Z. Cai, J.W. Shay, J. Yu, The cholesterol uptake regulator PCSK9 promotes and is a therapeutic target in APC/KRAS-mutant colorectal cancer, *Nat. Commun.* 13 (2022) 3971, <https://doi.org/10.1038/s41467-022-31663-z>.
- [10] A.D. Cox, S.W. Fesik, A.C. Kimmelman, J. Luo, C.J. Der, Drugging the undruggable RAS: mission possible? *Nat. Rev. Drug Discov.* 13 (2014) 828–851, <https://doi.org/10.1038/nrd4389>.
- [11] M.B. Ryan, R.B. Corcoran, Therapeutic strategies to target RAS-mutant cancers, *Nat. Rev. Clin. Oncol.* 15 (2018) 709–720, <https://doi.org/10.1038/s41571-018-0105-0>.
- [12] M. Malumbres, M. Barbacid, Ras oncogenes: The first 30 years, *Nat. Rev. Cancer* 3 (2003) 459–465, <https://doi.org/10.1038/nrc1097>.
- [13] R.P. Jones, P.A. Sutton, J.P. Evans, R. Clifford, A. McAvoy, J. Lewis, A. Rousseau, R. Mountford, D. McWhirter, H.Z. Malik, Specific mutations in KRAS codon 12 are associated with worse overall survival in patients with advanced and recurrent colorectal cancer, *Br. J. Cancer* 116 (2017) 923–929, <https://doi.org/10.1038/bjc.2017.37>.
- [14] M. Schirripa, F. Nappo, C. Cremolini, L. Salvatore, D. Rossini, M. Bensi, G. Businello, F. Pietrantonio, G. Randon, G. Fucà, A. Boccaccino, F. Bergamo, S. Lonardi, A.P. Dei Tos, M. Fassan, F. Loupakis, KRAS G12C metastatic colorectal cancer: specific features of a new emerging target population, *Clin. Colorectal Cancer* 19 (2020) 219–225, <https://doi.org/10.1016/j.clcc.2020.04.009>.
- [15] J.T. Henry, O. Coker, S. Chowdhury, J.P. Shen, V.K. Morris, A. Dasari, K. Raghav, M. Nusrat, B. Kee, C. Parseghian, S. Pant, N. Jeyakumar, L. Zhu, Y. Nishioka, D. Fogelman, R.A. Wolff, D. Hong, M.J. Overman, J. Vauthey, S. Kopetz, B. Johnson, Comprehensive clinical and molecular characterization of KRAS (G12C)-mutant colorectal cancer, *JCO Precis Oncol* 5 (2021), <https://doi.org/10.1200/po.20.00256>.
- [16] M.E. Salem, S.M. El-Refai, W. Sha, A. Puccini, A. Grothey, T.J. George, J.J. Hwang, B. O'Neil, A.S. Barrett, K.C. Kadakia, L.W. Musselwhite, D. Raghavan, E. Van Cutsem, J. Tabernero, Tie J, landscape of KRAS(G12C), associated genomic alterations, and interrelation with immuno-oncology biomarkers in KRAS-mutated cancers, *JCO Precis Oncol* 6 (2022), e2100245, <https://doi.org/10.1200/po.21.00245>.
- [17] M.R. Janes, J. Zhang, L.S. Li, R. Hansen, U. Peters, X. Guo, Y. Chen, A. Babbar, S. J. Firdaus, L. Darjania, J. Feng, J.H. Chen, S. Li, S. Li, Y.O. Long, C. Thach, Y. Liu, A. Zariah, T. Ely, J.M. Kucharski, L.V. Kessler, T. Wu, K. Yu, Y. Wang, Y. Yao, X. Deng, P.P. Zarrinkar, D. Brehmer, D. Dhanak, M.V. Lorenzi, D. Hu-Lowe, M. P. Patricelli, P. Ren, Y. Liu, Targeting KRAS mutant cancers with a covalent G12C-specific inhibitor, *Cell* 172 (2018) 578–589.e517, <https://doi.org/10.1016/j.cell.2018.01.006>.
- [18] D.S. Hong, M.G. Fakih, J.H. Strickler, J. Desai, G.A. Durm, G.I. Shapiro, G. S. Falchook, T.J. Price, A. Sacher, C.S. Denlinger, Y.J. Bang, G.K. Dy, J.C. Krauss, Y. Kuboki, J.C. Kuo, A.L. Coveler, K. Park, T.W. Kim, F. Barlesi, P.N. Munster, S. S. Ramalingam, T.F. Burns, F. Meric-Bernstam, H. Henary, J. Ngang, G. Ngarmchamnarnrith, J. Kim, B.E. Houk, J. Canon, J.R. Lipford, G. Friberg, P. Lito, R. Govindan, B.T. Li, KRAS(G12C) inhibition with sotorasib in advanced solid tumors, *N. Engl. J. Med.* 383 (2020) 1207–1217, <https://doi.org/10.1056/NEJMoa1917239>.
- [19] F. Skoulidis, B.T. Li, G.K. Dy, T.J. Price, G.S. Falchook, J. Wolf, A. Italiano, M. Schuler, H. Borghaei, F. Barlesi, T. Kato, A. Curioni-Fontecedro, A. Sacher, A. Spira, S.S. Ramalingam, T. Takahashi, B. Besse, A. Anderson, A. Ang, Q. Tran, O. Mather, H. Henary, G. Ngarmchamnarnrith, G. Friberg, V. Velcheti, R. Govindan, Sotorasib for lung cancers with KRAS p.G12C mutation, *N. Engl. J. Med.* 384 (2021) 2371–2381, <https://doi.org/10.1056/NEJMoa2103695>.
- [20] M.G. Fakih, S. Kopetz, Y. Kuboki, T.W. Kim, P.N. Munster, J.C. Krauss, G. S. Falchook, S.W. Han, V. Heinemann, K. Muro, J.H. Strickler, D.S. Hong, C. S. Denlinger, G. Girotto, M.A. Lee, H. Henary, Q. Tran, J.K. Park, G. Ngarmchamnarnrith, H. Prenen, T.J. Price, Sotorasib for previously treated colorectal cancers with KRAS(G12C) mutation (CodeBreak100): a prespecified analysis of a single-arm, phase 2 trial, *Lancet Oncol.* 23 (2022) 115–124, [https://doi.org/10.1016/s1470-2045\(21\)00605-7](https://doi.org/10.1016/s1470-2045(21)00605-7).
- [21] M.M. Awad, S. Liu, Rybkin II, K.C. Arbour, J. Dilly, V.W. Zhu, M.L. Johnson, R. S. Heist, T. Patil, G.J. Riely, J.O. Jacobson, X. Yang, N.S. Persky, D.E. Root, K. E. Lowder, H. Feng, S.S. Zhang, K.M. Haigis, Y.P. Hung, L.M. Sholl, B.M. Wolpin, J. Wiese, J. Christiansen, J. Lee, A.B. Schrock, L.P. Lim, K. Garg, M. Li, L. D. Engstrom, L. Waters, J.D. Lawson, P. Olson, P. Lito, S.I. Ou, J.G. Christensen, P. A. Jänne, A.J. Aguirre, Acquired resistance to KRAS(G12C) inhibition in cancer, *N. Engl. J. Med.* 384 (2021) 2382–2393, <https://doi.org/10.1056/NEJMoa2105281>.
- [22] N. Tanaka, J.J. Lin, C. Li, M.B. Ryan, J. Zhang, L.A. Kiedrowski, A.G. Michel, M. U. Syed, K.A. Fella, M. Sakhi, I. Baiev, D. Juric, J.F. Gainor, S.J. Klemperer, J. K. Lennerz, G. Siravegna, L. Bar-Peled, A.N. Hata, R.S. Heist, R.B. Corcoran, Clinical acquired resistance to KRAS(G12C) inhibition through a novel KRAS switch-II pocket mutation and polyclonal alterations converging on RAS-MAPK reactivation, *Cancer Discov.* 11 (2021) 1913–1922, <https://doi.org/10.1158/2159-8290.Cd-21-0365>.
- [23] Y. Zhao, Y.R. Murciano-Goroff, J.Y. Xue, A. Ang, J. Lucas, T.T. Mai, A.F. Da Cruz Paula, A.Y. Saiki, D. Mohn, P. Achanta, A.E. Sisk, K.S. Arora, R.S. Roy, D. Kim, C. Li, L.P. Lim, M. Li, A. Bahr, B.R. Loomis, E. de Stanchina, J.S. Reis-Filho, B. Weigelt, M. Berger, G. Riely, K.C. Arbour, J.R. Lipford, B.T. Li, P. Lito, Diverse alterations associated with resistance to KRAS(G12C) inhibition, *Nature* 599 (2021) 679–683, <https://doi.org/10.1038/s41586-021-04065-2>.
- [24] J. Datta, A. Bianchi, I. De Castro Silva, N.U. Deshpande, L.L. Cao, S. Mehra, S. Singh, C. Rafie, X. Sun, X. Chen, X. Dai, A. Colaprico, P. Sharma, A.R. Dosch, A. Pillai, P.J. Hosein, N.S. Nagathihalli, K.V. Komanduri, J.M. Wilson, Y. Ban, N. B. Merchant, Distinct mechanisms of innate and adaptive immune regulation underlie poor oncologic outcomes associated with KRAS-TP53 co-alteration in pancreatic cancer, *Oncogene* 41 (2022) 3640–3654, <https://doi.org/10.1038/s41388-022-02368-w>.
- [25] J. Datta, J.J. Smith, W.K. Chatila, J.C. McAuliffe, C. Kandoth, E. Vakiani, T. L. Frankel, K. Ganesh, I. Wasserman, M. Lipsyc-Sharf, J. Guillem, G.M. Nash, P. B. Paty, M.R. Weiser, L.B. Saltz, M.F. Berger, W.R. Jarnagin, V. Balachandran, T. P. Kingham, N.E. Kemeny, A. Cercek, J. Garcia-Aguilar, B.S. Taylor, A. Viale, R. Yaeger, D.B. Solit, N. Schultz, M.I. D'Angelica, Coaltered ras/B-raf and TP53 is associated with extremes of survivorship and distinct patterns of metastasis in patients with metastatic colorectal cancer, *Clin. Cancer Res.* 26 (2020) 1077–1085, <https://doi.org/10.1158/1078-0432.CCR-19-2390>.
- [26] S. Xiong, D. Chachad, Y. Zhang, J. Gencel-Augusto, M. Srito, V. Pant, P. Yang, C. Sun, G. Chau, Y. Qi, X. Su, E.M. Whitley, A.K. El-Naggar, G. Lozano, Differential gain-of-function activity of three p53 hotspot mutations in vivo, *Cancer Res.* 82 (2022) 1926–1936, <https://doi.org/10.1158/0008-5472.Can-21-3376>.
- [27] J. Zhu, M.A. Sammons, G. Donahue, Z. Dou, M. Vedadi, M. Getlik, D. Barsyte-Lovejoy, R. Al-awar, B.W. Katona, A. Shilatfard, J. Huang, X. Hua, C. H. Arrowsmith, S.L. Berger, Gain-of-function p53 mutants co-opt chromatin pathways to drive cancer growth, *Nature* 525 (2015) 206–211, <https://doi.org/10.1038/nature15251>.
- [28] V.J.N. Bykov, S.E. Eriksson, J. Bianchi, K.G. Wiman, Targeting mutant p53 for efficient cancer therapy, *Nat. Rev. Cancer* 18 (2018) 89–102, <https://doi.org/10.1038/nrc.2017.109>.
- [29] K. Sabapathy, D.P. Lane, Therapeutic targeting of p53: all mutants are equal, but some mutants are more equal than others, *Nat. Rev. Clin. Oncol.* 15 (2018) 13–30, <https://doi.org/10.1038/nrclinonc.2017.151>.
- [30] J. Wang, C. Qu, X. Shao, G. Song, J. Sun, D. Shi, R. Jia, H. An, H. Wang, Carrier-free nanoprodur for p53-mutated tumor therapy via concurrent delivery of zinc-manganese dual ions and ROS, *Bioact. Mater.* 20 (2023) 404–417, <https://doi.org/10.1016/j.bioactmat.2022.06.005>.
- [31] E. Ingallina, G. Sorrentino, R. Bertolio, K. Lisek, A. Zannini, L. Azzolin, Severino Lu, D. Scaini, M. Mano, F. Mantovani, A. Rosato, S. Biccato, S. Piccolo, G. Del Sal, Mechanical cues control mutant p53 stability through a mevalonate-RhoA axis, *Nat. Cell Biol.* 20 (2018) 28–35, <https://doi.org/10.1038/s41556-017-0009-8>.
- [32] A. Parrales, A. Ranjan, S.V. Iyer, S. Padhye, S.J. Weir, A. Roy, T. Iwakuma, DNPA1 controls the fate of misfolded mutant p53 through the mevalonate pathway, *Nat. Cell Biol.* 18 (2016) 1233–1243, <https://doi.org/10.1038/ncb3427>.
- [33] Y. Zhang, X. Huang, L. Wang, C. Cao, H. Zhang, P. Wei, H. Ding, Y. Song, Z. Chen, J. Qian, S. Zhong, Z. Liu, M. Wang, W. Zhang, W. Jiang, J. Zeng, G. Yao, L.P. Wen, Glutathionylation-dependent proteasomal degradation of wide-spectrum mutant p53 proteins by engineered zeolitic imidazolate framework-8, *Biomaterials* 271 (2021), 120720, <https://doi.org/10.1016/j.biomaterials.2021.120720>.
- [34] J. Qian, W. Zhang, P. Wei, G. Yao, T. Yi, H. Zhang, H. Ding, X. Huang, M. Wang, Y. Song, S. Zhong, L. Yang, J. Gao, Z. Zhou, Lp Wen, Y. Zhang, Enhancing chemotherapy of p53-mutated cancer through ubiquitination-dependent proteasomal degradation of mutant p53 proteins by engineered ZnFe-4 nanoparticles, *Adv. Funct. Mater.* 30 (2020), <https://doi.org/10.1002/adfm.202001994>.
- [35] J. Kim, L. Yu, W. Chen, Y. Xu, M. Wu, D. Todorova, Q. Tang, B. Feng, L. Jiang, J. He, G. Chen, X. Fu, Y. Xu, Wild-type p53 promotes cancer metabolic switch by inducing PUMA-dependent suppression of oxidative phosphorylation, *Cancer Cell* 35 (2019) 191–203.e198, <https://doi.org/10.1016/j.ccell.2018.12.012>.
- [36] O.D. Maddocks, C.R. Berkers, S.M. Mason, L. Zheng, K. Blyth, E. Gottlieb, K. H. Vousden, Serine starvation induces stress and p53-dependent metabolic remodelling in cancer cells, *Nature* 493 (2013) 542–546, <https://doi.org/10.1038/nature11743>.

- [37] Y. Liu, W. Gu, The complexity of p53-mediated metabolic regulation in tumor suppression, *Semin. Cancer Biol.* 85 (2022) 4–32, <https://doi.org/10.1016/j.semcancer.2021.03.010>.
- [38] B. Niu, K. Liao, Y. Zhou, T. Wen, G. Quan, X. Pan, C. Wu, Application of glutathione depletion in cancer therapy: enhanced ROS-based therapy, ferroptosis, and chemotherapy, *Biomaterials* 277 (2021), 121110, <https://doi.org/10.1016/j.biomaterials.2021.121110>.
- [39] M. Wang, Z. Yang, Y. Song, P. Wei, N. Ishiwe, L. Wang, H. Zhang, M. Jing, M. Gao, L. Wen, Y. Zhang, Proteasomal and autophagy-mediated degradation of mutp53 proteins through mitochondria-targeting aggregation-induced-emission materials, *Acta Biomater.* 150 (2022) 402–412, <https://doi.org/10.1016/j.actbio.2022.07.057>.
- [40] J. Li, Y. Ye, Z. Liu, G. Zhang, H. Dai, J. Li, B. Zhou, Y. Li, Q. Zhao, J. Huang, J. Feng, S. Liu, P. Ruan, J. Wang, J. Liu, M. Huang, X. Liu, S. Yu, Z. Liang, L. Ma, X. Gou, G. Zhang, N. Chen, Y. Lu, C. Di, Q. Xia, J. Pan, R. Feng, Q. Cai, S. Su, Macrophage mitochondrial fission improves cancer cell phagocytosis induced by therapeutic antibodies and is impaired by glutamine competition, *Nature cancer* 3 (2022) 453–470, <https://doi.org/10.1038/s43018-022-00354-5>.
- [41] J. Li, Q. Xia, C. Di, C. Li, H. Si, B. Zhou, S. Yu, Y. Li, J. Huang, Y. Lu, M. Huang, H. Liang, X. Liu, Q. Zhao, Tumor cell-intrinsic CD96 mediates chemoresistance and cancer stemness by regulating mitochondrial fatty acid  $\beta$ -oxidation, *Adv. Sci.* 10 (2023), e2202956, <https://doi.org/10.1002/advs.202202956>.
- [42] J. Zielonka, J. Joseph, A. Sikora, M. Hardy, O. Ouari, J. Vasquez-Vivar, G. Cheng, M. Lopez, B. Kalyanaram, Mitochondria-targeted triphenylphosphonium-based compounds: syntheses, mechanisms of action, and therapeutic and diagnostic applications, *Chem. Rev.* 117 (2017) 10043–10120, <https://doi.org/10.1021/acs.chemrev.7b00042>.
- [43] D. Jana, Y. Zhao, Strategies for enhancing cancer chemodynamic therapy performance, *Explorations* 2 (2022), 20210238, <https://doi.org/10.1002/exp.20210238>.
- [44] Z. Xu, Q. Wang, H. Zhong, Y. Jiang, X. Shi, B. Yuan, N. Yu, S. Zhang, X. Yuan, S. Guo, Y. Yang, Carrier strategies boost the application of CRISPR/Cas system in gene therapy, *Explorations* 2 (2022), 20210081, <https://doi.org/10.1002/exp.20210081>.
- [45] S. Wu, K. Zhang, Y. Liang, Y. Wei, J. An, Y. Wang, J. Yang, H. Zhang, Z. Zhang, J. Liu, J. Shi, Nano-enabled tumor systematic energy exhaustion via zinc (II) interference mediated glycolysis inhibition and specific GLUT1 depletion, *Adv. Sci.* 9 (2022), e2103534, <https://doi.org/10.1002/advs.202103534>.
- [46] W. Wang, C. Chen, Y. Ying, S. Lv, Y. Wang, X. Zhang, Z. Cai, W. Gu, Z. Li, G. Jiang, F. Gao, Smart PdH@MnO(2) yolk-shell nanostructures for spatiotemporally synchronous targeted hydrogen delivery and oxygen-elevated phototherapy of melanoma, *ACS Nano* 16 (2022) 5597–5614, <https://doi.org/10.1021/acsnano.1c10450>.
- [47] J. He, W. Zhang, X. Zhou, F. Xu, J. Zou, Q. Zhang, Y. Zhao, H. He, H. Yang, J. Liu, Reactive oxygen species (ROS)-responsive size-reducible nanoassemblies for deeper atherosclerotic plaque penetration and enhanced macrophage-targeted drug delivery, *Bioact. Mater.* 19 (2023) 115–126, <https://doi.org/10.1016/j.bioactmat.2022.03.041>.
- [48] S. Shen, X. Xu, S. Lin, Y. Zhang, H. Liu, C. Zhang, R. Mo, A nanotherapeutic strategy to overcome chemotherapeutic resistance of cancer stem-like cells, *Nat. Nanotechnol.* 16 (2021) 104–113, <https://doi.org/10.1038/s41565-020-00793-0>.
- [49] G. Zhu, L. Pei, H. Xia, Q. Tang, F. Bi, Role of oncogenic KRAS in the prognosis, diagnosis and treatment of colorectal cancer, *Mol. Cancer* 20 (2021) 143, <https://doi.org/10.1186/s12943-021-01441-4>.
- [50] S.R. Singh, M. Meyer-Jens, E. Alizoti, W.C. Bacon, G. Davis, H. Osinska, J. Gulick, S. Reischmann-Düsener, E. Orthey, P.M. McLendon, J.D. Molkenin, S. Schlossarek, J. Robbins, L. Carrier, A high-throughput screening identifies ZNF418 as a novel regulator of the ubiquitin-proteasome system and autophagy-lysosomal pathway, *Autophagy* 17 (2021) 3124–3139, <https://doi.org/10.1080/15548627.2020.1856493>.
- [51] D. Ebrahimi-Fakhari, I. Cantuti-Castelvetri, Z. Fan, E. Rockenstein, E. Masliah, B. T. Hyman, P.J. McLean, V.K. Unni, Distinct roles in vivo for the ubiquitin-proteasome system and the autophagy-lysosomal pathway in the degradation of  $\alpha$ -synuclein, *J. Neurosci.* 31 (2011) 14508–14520, <https://doi.org/10.1523/jneurosci.1560-11.2011>.
- [52] Y. Yang, J. Kitagaki, R.M. Dai, Y.C. Tsai, K.L. Lorick, R.L. Ludwig, S.A. Pierre, J. P. Jensen, I.V. Davydov, P. Oberoi, C.C. Li, J.H. Kenten, J.A. Beutler, K.H. Vousden, A.M. Weissman, Inhibitors of ubiquitin-activating enzyme (E1), a new class of potential cancer therapeutics, *Cancer Res.* 67 (2007) 9472–9481, <https://doi.org/10.1158/0008-5472.Can-07-0568>.
- [53] M. Nakayama, C.P. Hong, H. Oshima, E. Sakai, S.J. Kim, M. Oshima, Loss of wild-type p53 promotes mutant p53-driven metastasis through acquisition of survival and tumor-initiating properties, *Nat. Commun.* 11 (2020) 2333, <https://doi.org/10.1038/s41467-020-16245-1>.
- [54] X. Yue, Y. Zhao, J. Liu, C. Zhang, H. Yu, J. Wang, T. Zheng, L. Liu, J. Li, Z. Feng, W. Hu, BAG2 promotes tumorigenesis through enhancing mutant p53 protein levels and function, *Elife* 4 (2015), <https://doi.org/10.7554/eLife.08401>.
- [55] C. Zhang, J. Liu, D. Xu, T. Zhang, W. Hu, Z. Feng, Gain-of-function mutant p53 in cancer progression and therapy, *J. Mol. Cell Biol.* 12 (2020) 674–687, <https://doi.org/10.1093/jmcb/mjaa040>.
- [56] O. Hassin, M. Oren, Drugging p53 in cancer: one protein, many targets, *Nat. Rev. Drug Discov.* 22 (2023) 127–144, <https://doi.org/10.1038/s41573-022-00571-8>.
- [57] M. Izci, C. Maksoudian, B.B. Manshian, S.J. Soenen, The use of alternative strategies for enhanced nanoparticle delivery to solid tumors, *Chem. Rev.* 121 (2021) 1746–1803, <https://doi.org/10.1021/acs.chemrev.0c00779>.
- [58] P. Nallasamy, R.K. Nimmakayala, S. Karmakar, F. Leon, P. Seshacharyulu, I. Lakshmanan, S. Rachagani, K. Mallya, C. Zhang, Q.P. Ly, M.S. Myers, L. Josh, C. E. Grabow, S.K. Gautam, S. Kumar, S.M. Lele, M. Jain, S.K. Batra, M.P. Ponnusamy, Pancreatic tumor microenvironment factor promotes cancer stemness via SPP1-CD44 Axis, *Gastroenterology* 161 (2021) 1998–2013.e1997, <https://doi.org/10.1053/j.gastro.2021.08.023>.
- [59] Y. Wang, D. Gao, Y. Liu, X. Guo, S. Chen, L. Zeng, J. Ma, X. Zhang, Z. Tian, Z. Yang, Immunogenic-cell-killing and immunosuppression-inhibiting nanomedicine, *Bioact. Mater.* 6 (2021) 1513–1527, <https://doi.org/10.1016/j.bioactmat.2020.11.016>.
- [60] X. Zhang, J. Tang, C. Li, Y. Lu, L. Cheng, J. Liu, A targeting black phosphorus nanoparticle based immune cells nano-regulator for photodynamic/photothermal and photo-immunotherapy, *Bioact. Mater.* 6 (2021) 472–489, <https://doi.org/10.1016/j.bioactmat.2020.08.024>.
- [61] L.F. Escobar-Hoyos, A. Penzon, R. Kannan, H. Cho, C.H. Pan, R.K. Singh, L. H. Apken, G.A. Hobbs, R. Luo, N. Lecomte, S. Babu, F.C. Pan, D. Alonso-Curbelo, J.P. Morris, G. Askan, O. Grbovic-Huezo, P. Ogradowski, J. Bermeo, J. Saglimbeni, C.D. Cruz, Y.J. Ho, S.A. Lawrence, J.P. Melchor, G.A. Goda, K. Bai, A. Pastore, S. J. Hogg, S. Raghavan, P. Bailey, D.K. Chang, A. Biankin, K.R. Shroyer, B.M. Wolpin, A.J. Aguirre, A. Ventura, B. Taylor, C.J. Der, D. Dominguez, D. Kümmel, A. Oeckinghaus, S.W. Lowe, R.K. Bradley, O. Abdel-Wahab, S.D. Leach, Altered RNA splicing by mutant p53 activates oncogenic RAS signaling in pancreatic cancer, *Cancer Cell* 38 (2020) 198–211.e198, <https://doi.org/10.1016/j.ccell.2020.05.010>.
- [62] M.P. Kim, X. Li, J. Deng, Y. Zhang, B. Dai, K.L. Allton, T.G. Hughes, C. Siangco, J. J. Augustine, Y. Kang, J.M. McDaniel, S. Xiong, E.J. Koay, F. McAllister, C. A. Bristow, T.P. Heffernan, A. Maitra, B. Liu, M.C. Barton, A.R. Wasylshen, J. B. Fleming, G. Lozano, Oncogenic KRAS recruits an expansive transcriptional network through mutant p53 to drive pancreatic cancer metastasis, *Cancer Discov.* 11 (2021) 2094–2111, <https://doi.org/10.1158/2159-8290.Cd-20-1228>.